Quantum Spin-Ice and Dimer Models with Rydberg Atoms

A. W. Glaetzle,[1,2,*] M. Dalmonte,[1,2] R. Nath,[1,2,3] I. Rousochatzakis,[4] R. Moessner,[4] and P. Zoller[1,2]

[1]*Institute for Quantum Optics and Quantum Information of the Austrian Academy of Sciences,
A-6020 Innsbruck, Austria*
[2]*Institute for Theoretical Physics, University of Innsbruck, A-6020 Innsbruck, Austria*
[3]*Indian Institute of Science Education and Research, Pune 411 008, India*
[4]*Max Planck Institute for the Physics of Complex Systems, D-01187 Dresden, Germany*

Quantum spin-ice represents a paradigmatic example of how the physics of frustrated magnets is related to gauge theories. In the present work, we address the problem of approximately realizing quantum spin ice in two dimensions with cold atoms in optical lattices. The relevant interactions are obtained by weakly laser-admixing Rydberg states to the atomic ground-states, exploiting the strong angular dependence of van der Waals interactions between Rydberg p states together with the possibility of designing steplike potentials. This allows us to implement Abelian gauge theories in a series of geometries, which could be demonstrated within state-of-the-art atomic Rydberg experiments. We numerically analyze the family of resulting microscopic Hamiltonians and find that they exhibit both classical and quantum order by disorder, the latter yielding a quantum plaquette valence bond solid. We also present strategies to implement Abelian gauge theories using both s- and p-Rydberg states in exotic geometries, e.g., on a 4–8 lattice.

Subject Areas: Atomic and Molecular Physics,
Condensed Matter Physics

I. INTRODUCTION

The ice model has been fundamental in furthering our understanding of collective phenomena in condensed matter and statistical physics: In 1935, Pauling provided an explanation of the "zero-point entropy' of water ice [1] as measured by Giauque and Stout [2], while Lieb demonstrated, with his exact solution of the ice model in two dimensions [3], that there exist phase transitions with critical exponents that are different from those of Onsager's solution of the Ising model. The experimental discovery [4] of a classical spin version of the ice model [5] has, in turn, generated much interest in the magnetism community [6–9].

More recently, quantum-ice models [10–14] have attracted a great deal of attention in the context of phases exhibiting exotic types of orders, such as resonating valence bond liquids [15,16] or quantum Coulomb phases [12,17–19]. They form part of a broader family of models, which also includes quantum dimer models or other quantum vertex models [20], in which a hard constraint is imposed locally, such as the ice rules defined below. Such a constraint can then endow the configuration space with additional structure—most prominently, an emergent

gauge field that can be the basis of the appropriate effective description at low energies [20–22]. This is an important phenomenon, as it is perhaps the simplest way of obtaining gauge fields as effective degrees of freedom in condensed matter physics. More broadly, this is part of a long-running search for magnetic materials hosting quantum spin liquids [7].

In the present work, we address the problem of physically realizing models of quantum spin-ice and quantum dimer models in two spatial dimensions with ultracold atoms in optical lattices. Our proposal builds on the recent experimental advances, and opportunities in engineering many-body interactions with laser-excited Rydberg states [23–37]. In particular, this will allow us to develop a Rydberg toolbox for the complex interactions required in two-dimensional (2D) quantum-ice models [8]. Our investigation also fits into the broader quest for the realization of synthetic gauge fields with cold atoms. While much effort is being devoted to the generation of static gauge fields [38], e.g., on optical flux lattices, here we follow the strategy of generating a *dynamical* gauge field [12,17–19,21,22,39–42] emerging upon imposition of the ice rule.

While in condensed matter systems the interactions underlying ice and spin ice arise naturally in a three-dimensional (3D) context [see Fig. 1(a)], the 2D quantum ice on a square lattice requires a certain degree of fine-tuning of the relevant interactions [see Fig. 1(b)]. In 3D spin-ice materials, for example, the ions of magnetic rare-earth atoms reside on a pyrochlore lattice, representing a

network of corner-sharing tetrahedra. Magnetic interactions in combination with crystal fields give rise to a low-energy manifold of states on each tetrahedron consisting of six configurations, in which two spins point inward and two spins point outward [compare Fig. 1(c)]. In a similar way, in water ice each O^{2-} atom in a tetrahedrally coordinated framework has two protons attached to it, giving rise to a manifold of energetically degenerate configurations. The 2D models of ice and spin ice can be understood as the projection of the pyrochlore on a square lattice (see Fig. 1), where again the low-energy configurations of spins residing on the links obey the "ice rule" 2 in and 2 out at each vertex. While these 2D ice models play a fundamental role in our theoretical understanding of frustrated materials, a physical realization requires a precise adjustment of the underlying interactions—different local configurations that are symmetry distinct need to be at least approximately degenerate; the required fine-tuning, however, needs to be delicately directionally dependent, as in the pure ice model, the ratio of some interactions between different pairs of

equidistant spins vanishes [see Fig. 1(b)]. Things are not all hopeless, however, as there exist a number of settings in which partial progress has been made to realizing such models. In two dimensions, artificial structures using nanomagnetic [43] or colloidal arrays [44] have been proposed, including strategies for tuning the interactions appropriately [45]. The present proposal with Rydberg atoms is unique, however, as it combines both the possibilities of engineering the complex interactions using Rydberg interactions with the accessibility of the quantum regime in cold-atom experiments.

Alkali atoms prepared in their electronic ground state can be excited by laser light to Rydberg states, i.e., states of high principal quantum number n [46–49]. These Rydberg atoms interact strongly via the van der Waals (vdW) interaction, exhibiting the remarkable scaling $V_{\text{VdW}} \sim n^{11}$, and exceeding typical ground-state interactions of cold atoms by several orders of magnitude. In an atomic ensemble, the large level shifts associated with these interactions imply that only a single atom can be excited to the Rydberg state, while multiple excitations are suppressed within a blockade radius determined by the van der Waals interactions and laser parameters [50,51]. This blockade mechanism results in novel collective and strongly correlated many-particle phenomena such as the formation of superatoms and Rydberg quantum crystals [46–49]. In present experiments, the emphasis is on *isotropic* van der Waals interactions [23–36], which, for example, can be obtained by exciting Rydberg s states using a two-photon excitation scheme. In contrast, we are interested below in excitations of Rydberg p states, where the van der Waals interactions can be highly *anisotropic*, as discussed in Refs. [52–55]. Below, we will discuss in detail the controllability of the shape and range of these anisotropic interactions via atomic and laser parameters for the case of Rb atoms. In the present context, this will provide us with the tools to engineer the required complex interaction patterns for 2D quantum spin-ice and dimer models. The setup we discuss will consist of cold atoms in optical lattices, where the strong Rydberg interactions are weakly admixed to the atomic ground states [56–60], thus effectively dressing ground-state atoms to obtain the complex interactions in atomic Hubbard models required for the realization of 2D quantum spin-ice and dimer models.

We then proceed to numerically analyze the family of Hamiltonians realizable with this toolbox. We verify that it contains two phases exhibiting distinct types of order by disorder [61,62]. Most remarkably, quantum order by disorder—due to the presence of quantum dynamics in the ice model—realizes the plaquette valence bond solid as an unusual non-Néel phase of a frustrated magnet. This terminates when classical degeneracy lifting takes over.

The latter phase is conventional in that it is diagnosed by a conventional spin-order parameter, which would manifest itself in a Bragg peak in the structure factor. By contrast, the valence bond solid would be diagnosed by higher-order
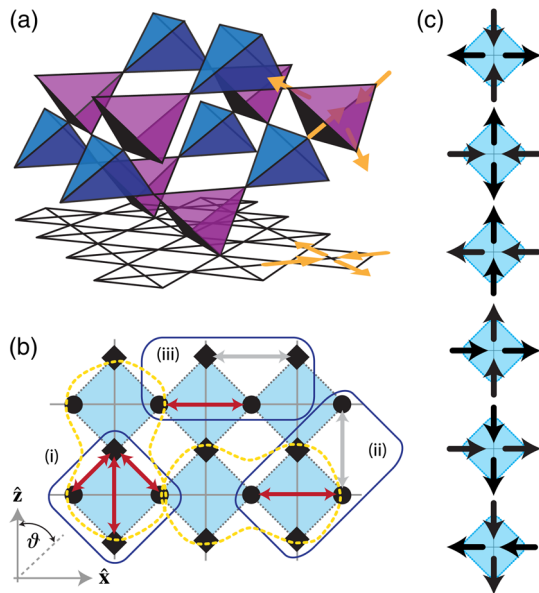

FIG. 1. (a) In spin-ice materials, the magnetic moments (yellow arrows) of rare-earth ions are located on the corners of a pyrochlore lattice, which is a network of corner-sharing tetrahedra. They behave as almost perfect Ising spins and point along the line from the corner to the center of the tetrahedron, either inward or outward. Because of the different Ising axes of the spins, this results in an effectively antiferromagnetic interaction that is frustrated. (b) Projecting the 3D pyrochlore lattice onto a 2D square lattice yields a checkerboard lattice, where tetrahedrons are mapped onto crossed plaquettes (light blue). Interactions between two spins located on ● or ■ lattice sites have to be steplike (as a function of the distance) and anisotropic, and they require a bipartite labeling of the lattice sites. (c) Degenerate ground-state configurations of spins on a crossed plaquette. They obey the "ice rules," which enforce two spins pointing inward and two spins pointing outward at each vertex.

"string" correlators, and it is thus fundamentally different from some other instances of quantum order by disorder, where finally the mechanism, but not quite so much the order parameter, is exotic [62,63]. Notably, precisely such order parameters have become accessible to experimental measurements recently [64], so our proposal not only covers the setting for realizing quantum order by disorder but also the means for detecting it.

In addition, at finite temperature, we find that the classically ordered state, even in the absence of quantum dynamics, melts into a classical version of a Coulomb phase, namely, a Coulomb gas in which thermally activated plaquettes violating the ice rule play the role of positive and negative charges. As these interact via an entropic two-dimensional (logarithmic) Coulomb law, this phase is only marginally confined [65,66].

While throughout the paper we will mostly be interested in quantum-ice models, which require the development of advanced interaction-pattern design, we will also discuss a second strategy to implement constrained dynamics, and, in particular, quantum dimer models, with Rydberg atoms. It relies on combining simple interaction patterns, such as the ones generated by s states, with complex lattice structures, which can be realized either via proper laser combination or by the recently developed optical lattice design with digital micromirror devices [67]. These models extend the class of dynamical gauge fields in atomic, molecular, and optical physics (AMO) systems to nonhypercubic geometries. Overall, the ability to synthetically design Abelian dynamical gauge fields with discrete variables also establishes interesting connections with high-energy physics, where these theories are usually referred to as quantum link models [68,69]. Within this context, the key developments in engineering pure gauge theories can be combined with other schemes (where dynamical matter is included), which have already been proposed in the context of cold-atom gases [69].

The paper is structured as follows. In Sec. II, we briefly provide the background on quantum-ice models needed for digesting the remainder of the material. Section III outlines the implementation of a family of model Hamiltonians approximating the quantum-ice model using atoms in optical lattices that are weakly admixed with a Rydberg p state. Our model Hamiltonians are then analyzed for their phase diagram in Sec. IV. Section V presents strategies to implement simpler Abelian gauge theories using both s- and p-Rydberg states in exotic geometries, e.g., a 4–8 lattice. The paper closes with a summary and outlook in Sec. VI.

II. THE QUANTUM-ICE MODEL

This section provides a brief overview of the statistical mechanics of the ice model, the emergence of a gauge field, and the challenges in realizing such a model experimentally.

A. The configuration space: Ice rules and emergent gauge fields

The ice model on the square lattice, also known as the six-vertex model or simply square ice [3], has Ising degrees of freedom residing on the *links* of a square lattice. They can either be thought of as fluxes, $\{\hat{S}_i^z\}$, pointing in either of the directions along the bond i [see layer (i) of Fig. 2(a)], or equivalently, they can be mapped onto spins $\{S_i^z\}$ that point up or down depending on the direction of the flux [see layer (ii) of Fig. 2(a)].

Only configurations satisfying the ice rule are permitted, which stipulates that the spins on each vertex add up to zero—there are $\binom{4}{2} = 6$ ways of arranging this [see panel (i) of Fig. 2(b)]. The number of configurations satisfying the ice rule grows exponentially with the size of the system—for a lattice of N spins, there are $(4/3)^{(3N/4)}$ ice states [3].

The origin of the emergent gauge field is transparent in flux language, where it implies that the lattice divergence of the flux field vanishes: Defining the $x(y)$ component of a
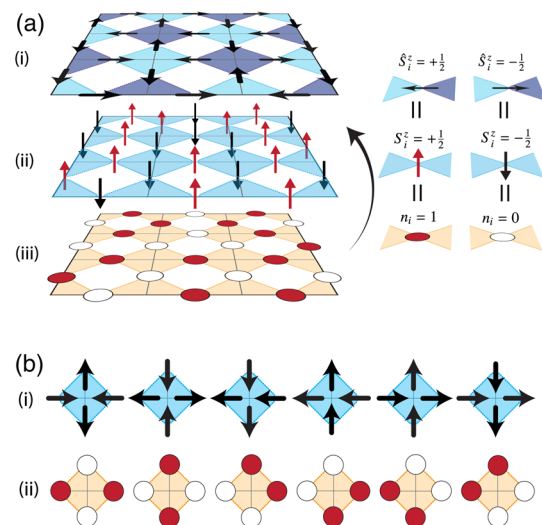

FIG. 2.   (a) The spins of the 2D ice model on a checkerboard lattice can be interpreted as (i) "fluxes," $\{\hat{S}_i^z\}$, pointing either inward or outward from a specific crossed plaquette. This requires a bipartite labeling of the plaquettes (light blue and light magenta plaquettes) since an outward-pointing flux vector corresponds to an inward-pointing flux vector for the neighboring plaquette. (ii) They can be interpreted as spins, $\{S_i^z\}$, aligned perpendicular to the plane, pointing either up (red arrows) or down (black arrows). In the right inset, we identify a spin pointing up, $S_i^z = +\frac{1}{2}$, with a flux vector pointing from the magenta to the blue plaquette, $\hat{S}_i^z = +\frac{1}{2}$ and vice versa. (iii) Spins, $\{S_i^z\}$, can be mapped onto hard-core bosons, $n_i \in \{0, 1\}$. Here, e.g., a particle (red circle), $n_i = 1$, corresponds to a spin pointing upward, $S_i^z = +\frac{1}{2}$, while an empty lattice site (white circle), $n_i = 0$, corresponds to a spin pointing downward, $S_i^z = -\frac{1}{2}$. (b) The six *ice-rule* states correspond to vertex configurations with two hard-core bosons and two empty lattice sites.

two-dimensional vector flux **b** to be the flux along the corresponding links emanating from a vertex in the positive $x(y)$ direction, one has

$$\nabla \cdot \mathbf{b} = 0 \Rightarrow \mathbf{b} = \nabla \times \mathbf{a}. \qquad (1)$$

Note that a gauge field **a** has appeared naturally as a consequence of enforcing the ice rule, just as it does in magnetostatics, where Maxwell's law for the magnetic field $\nabla \cdot \mathbf{B} = 0$ leads to the introduction of the familiar vector potential **A**.

In the present example in two dimensions, where the flux is a two-component vector **b**, and the scalar constraint $\nabla \cdot \mathbf{b} = 0$ fixes 1 degree of freedom, **a** only has one physical degree of freedom left—it can be thought of as a scalar, usually referred to as a height: $\mathbf{a} = h\mathbf{z}$ "in the z direction" [65,66]. Defects in this height field—forbidden in the six-vertex model but allowed when violating the ice rule results in only a finite energy penalty—are then known as charges or monopoles, which carry a gauge charge with respect to the emergent gauge field.

Having enforced the ice rule, the natural degree of freedom is thence an *emergent* gauge field **a**—it is in this way that gauge fields quite generically emerge in condensed matter physics, with a constraint arising either from the need to satisfy a dominant term in the Hamiltonian or from a microscopic relation on the local Hilbert space [20].

B. Realization, and fine-tuning in $d = 2$

The ice rule on a given vertex involves four spins, but it can be enforced via a pairwise interaction: If all four spins on a vertex interact antiferromagnetically *and equally*—described by the Hamiltonian

$$H_{\text{ice}} = V \sum_{i,j \in +} S_i^z S_j^z, \qquad (2)$$

where $+$ denotes a crossed plaquette in 2D or a tetrahedron in 3D—the resulting ground states are those which obey the ice rules [see panel (i) of Fig. 2(b)]. In three dimensions, equality of the pairwise interactions can be symmetry generated; by placing the spins on the corners of a tetrahedron, any antiferromagnetic interaction depending only on the distance between the spins will yield the ice rule. By contrast, in two dimensions, a tetrahedron becomes a square with interactions also across the diagonal (Fig. 1), which are no longer symmetry equivalent to those along the edges [70].

In particular, interactions, $V_{ij}(\mathbf{r})$, between two spins i and j located on the bonds of a checkerboard lattice separated by a distance **r** have to fulfill three demanding properties [see Fig. 1(b)] in order to map onto the spin-ice Hamiltonian of Eq. (2) 1. *Anisotropy*. Interactions have to be strongly anisotropic. This is illustrated in panel (ii) of Fig. 1(b). Particles that belong to the same vertex interact

strongly (red arrow), while particles that do not belong to the same vertex do not interact (gray arrow). Thus, for ● particles in panel (ii), one needs an interaction that satisfies $V_{\bullet\bullet}(\vartheta = 0) = 0$ (gray arrow) and $V_{\bullet\bullet}(\vartheta = \pi/2) = \tilde{V}_0$ (red arrow), where the angle ϑ is defined in the inset. 2. *Steplike potentials*. All four particles that belong to the same vertex (enclosed by light blue squares) interact with the same strength $\tilde{V}_0$, independent of their distance, either a or $a\sqrt{2}$, where a is the lattice spacing. Obviously, an interaction of the form $1/|\mathbf{r}|^{\alpha}$ would not suffice. It is therefore necessary to have steplike potentials that fulfill $V_{ij}(|\mathbf{r}| < r_c) = \tilde{V}_0 \neq 0$ and $V_{ij}(|\mathbf{r}| > r_c) = 0$ for $\sqrt{2}a < r_c < 2a$. 3. *Bipartite-lattice structure*. Furthermore, panel (iii) of Fig. 1(b) shows that the desired interaction properties cannot be satisfied by a homogeneous interaction pattern, but require a bipartite structure [squares and circles in Fig. 1(b)] where the angular dependence on the interaction depends on the lattice bipartition. For example, in the last paragraph, we enforced that $V_{\bullet\bullet}(\vartheta = 0) = 0$ [see panel (ii)], but the opposite is true for ■ particles [see panel (iii)]. Here, $V_{\blacksquare\blacksquare}(\vartheta = \pi/2) = 0$ but $V_{\blacksquare\blacksquare}(\vartheta = 0) = \tilde{V}_0$. On top of that, mixed interactions between ● and ■ particles on the 45-degree lines should obey $V_{\bullet\blacksquare}(\vartheta = \pm\pi/4) = \tilde{V}_0$ in order to ensure that all six possible interactions at a specific vertex are the same [see panel (i)].

It is these three countervailing requirements that we manage to satisfy approximately by using Rydberg dressed atoms to engineer an appropriate quantum Hamiltonian (Sec. III).

C. Adding quantum dynamics, and quantum order by disorder

While the properties of the two-dimensional ice model were broadly understood a long time ago, the question of what a quantum version would look like was not posed until much later [10]. Unlike in, say, a transverse-field Ising model, where the simplest quantum dynamics consists of reversing a single spin, the ice model does not permit such single-site configuration changes, as these would lead to a violation of the ice rule.

The smallest cluster that may flip consists of a closed flux loop around an empty square plaquette, denoted by □ (see Fig. 3),

$$H_{\square} = -t \sum_{\substack{j \square k \\ i \square l}} (S_i^+ S_j^- S_k^+ S_l^- + \text{H.c.}), \qquad (3)$$

and this will be the second ingredient that our work will implement (Sec. III). What this amounts to in the language of gauge theory is the addition of a field conjugate to the height-gauge field $\mathbf{a} = h\mathbf{z}$—or in more familiar parlance of electromagnetism, the appearance of an (emergent) magnetic field alongside an (emergent) electric one [22].

In two dimensions, adapting a celebrated result by Polyakov (which does not apply straightforwardly as it
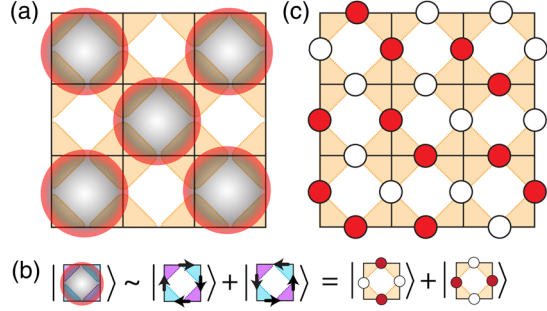
FIG. 3. (a) Cartoon state of a plaquette RVB solid. An alternating pattern of plaquettes (shaded red circles) are resonating; i.e., they are in an eigenstate $|\odot\rangle$ [see panel (b)] of the plaquette Hamiltonian of Eq. (3), $H_\square|\odot\rangle = -t|\odot\rangle$. The GS in the thermodynamic limit is twofold degenerate, reflecting the different coverings of the square lattice with alternating plaquettes. (c) Cartoon of one of the degenerate ground states with $(-\pi/2, \pi/2)$ order. Along the bottom-left and top-right diagonals, there is antiferromagnetic order. Along the other, the order has a double period, $\uparrow\uparrow\downarrow\downarrow$.

is based on Lorentz invariance which does not hold *a priori* for our emergent field), it is known that the (emergent) electromagnetism is confining. As a consequence, the emergent excitations cannot spread freely over the system, being bounded by an effective string tension due to the gauge fields. Concretely, one finds a phenomenon known as order by disorder [62]. The quantum dynamics mixes the degenerate ice states into a superposition to form the quantum ground state. Even though the quantum dynamics induces fluctuations ("disorder"), the resulting ground state exhibits long-range order. This order takes the form known as a plaquette valence bond solid (Fig. 3) [71], which breaks translational symmetry. Such valence bond solids occur frequently in the theory of quantum magnets, but they are not commonly realized in experiment.

In Sec. IV, we show that the model Hamiltonian for which we provide a recipe does exhibit this kind of order-by-disorder plaquette phase, and we discuss how to detect this kind of exotic order. In addition, we find that for weak quantum dynamics, a different, classical type of symmetry breaking occurs [see Fig. 3(c)]. This happens because different ice states are only approximately degenerate for our engineered Hamiltonian, and the residual energy differences are sufficient to select a particular ordered configuration.

D. Relation between quantum-ice, Bose-Hubbard models, and dimer models

As a starting point for our implementation, we consider a hard-core extended Bose-Hubbard Hamiltonian on a 2D checkerboard lattice:

$$H = -J_h \sum_{\langle i,j\rangle}(b_i^\dagger b_j + \text{H.c.}) + \sum_{i,j}\tilde{V}_{ij}n_in_j. \quad (4)$$

Here, $b_i^\dagger$ (b_i) is an operator that creates (annihilates) a hard-core boson on site i, which obeys an on-site constraint $b_i^2 = b_i^{\dagger 2} = 0$. The rate J_h is the nearest-neighbor (NN) hopping amplitude, and V describes a repulsion between all atoms sitting close to the same vertex. The operator $n_i = b_i^\dagger b_i$ counts the number of bosons at site i and can be either zero or one, $n_i \in \{0, 1\}$. The summation runs over nearest neighbors only. The hard-core boson model can be mapped to a spin-1/2 model using the transformation [72] $b_i^\dagger \to S_i^+$, $b_i \to S_i^-$, $n_i \to S_i^z + 1/2$, $J_h \to J_\perp$ and $V_{ij} \to J_{ij}$, which yields

$$H = -J_\perp\sum_{\langle ij\rangle}(S_i^+S_j^- + \text{H.c.})$$

$$+ \sum_{\langle ij\rangle}J_{ij}\left(S_i^z + \frac{1}{2}\right)\left(S_j^z + \frac{1}{2}\right). \quad (5)$$

Expanding the last term gives the two-body interaction proportional to $J_{ij}S_i^zS_j^z$ and an additional magnetic-field term proportional to $J_{ij}S_i^z$, which is constant after fixing an initial number of particles. This will fix the gauge sector in the gauge-theory description [20].

In order to implement the constrained model of Eq. (2), we demand (i) *anisotropic* and (ii) *steplike* interactions between (iii) *two species* of particles, as discussed in Sec. II B; that is, $\tilde{V}_{ij}$ has to fulfill

$$\sum_{ij}\tilde{V}_{ij}n_in_j = \tilde{V}_0\sum_{+}\sum_{i,j\in+}n_in_j, \quad (6)$$

with $\tilde{V}_0$ a constant interaction between all particles belonging to the same vertex denoted by $+$. Under these assumptions, in the limit $\tilde{V}_0 \gg J_h$, the Bose-Hubbard Hamiltonian of Eq. (4) maps onto the spin-ice Hamiltonian of Eq. (2). The specific form of V_{ij} ensures that all six interactions between particles that belong to the same vertex are equal, and interactions between particles that do not belong to the same vertex vanish. In the case of total half-filling of the initial bosons, $N = L/2$, one has $\sum_i S_i^z = 0$: This fixes the effective dynamics on the aforementioned ice manifold of interest. When different initial fillings are considered, one has access to different quantum dynamics: A notable case is the $N = L/4$ case, which defines a constrained dynamics on a manifold where a single boson sits close to each vertex [10]. The effective description is then the same as hard-code quantum dimer models on a square lattice.

III. QUANTUM ICE WITH RYDBERG-DRESSED ATOMS: EXPLOITING p STATES

We now turn to the realization of the extended 2D Bose-Hubbard Hamiltonian of Eq. (4) with cold atoms in optical lattices. The key challenge is the implementation of the interactions $\tilde{V}_{ij}$ with constraints represented in Eq. (6).

We show below that this can be achieved via the very anisotropic Rydberg interactions involving laser-excited p states of Rubidium atoms.

A. Single-particle Hamiltonian on a bipartite lattice

In our setup, we consider Rubidium ^{87}Rb atoms prepared in an internal ground state, which we choose as $|g\rangle \equiv |F = 2, m_F = 2\rangle$. The atoms are trapped in a 2D square optical lattice in the xz plane created by two pairs of counterpropagating laser beams of wavelength λ and wave vector $k = 2\pi/\lambda$, and strongly confined in the y direction by an additional laser. [We note that these external coordinates should not be confused with the internal spin coordinates, e.g., in Eq. (2) and Fig. 2]. By tilting the laser beams by an angle α, we can adjust the lattice spacing in the xz plane to any value $a = \lambda/[2\sin(\alpha/2)] \geq \lambda/2$ [73] (see below). Quantum tunneling allows the atoms to hop between different lattice sites, thus realizing the kinetic energy term with hopping amplitude J_h of the single-band Hubbard model (4). Furthermore, we work in the hard-core boson limit, i.e., $U \gg J_h$, in which multiple occupancy in a single site is energetically prohibited.

As already discussed in the context of Fig. 1(b), we want to distinguish between ● and ■ sites in the 2D lattice. This bipartite labeling of the optical lattice is essential for realizing the complex interaction pattern $\tilde{V}_{●●}$, $\tilde{V}_{●■}$, and $\tilde{V}_{■■}$ discussed in Sec. II B, which underlies the second term of the extended Bose-Hubbard Hamiltonian (4). In our scheme, we assume that atoms on lattice sites ● are excited by laser light to the Rydberg $^2P_{3/2}$ state $|r_●\rangle = |n^2P_{3/2},$

$m = 3/2\rangle_z$, whereas atoms at sites ■ are excited to $|r_■\rangle = |n^2P_{3/2}, m = 3/2\rangle_x$. Here, the subscripts x and z indicate the different local quantization axes for the ● and ■ sites. Note that the Rydberg states of interest are the stretched states of the fine-structure manifold, i.e., states with a maximum $m = 3/2$ value for the given angular momentum $j = 3/2$. We will show in the next section that the van der Waals interactions between these polarized Rydberg p states naturally realize the complex interaction pattern required by Eq. (6) for quantum spin-ice. By weakly admixing these Rydberg states to the atomic ground state with a laser [see Sec. III C], the ground-state atoms will inherit these interaction patterns, thus realizing the interaction term in the extended Bose-Hubbard model of Eq. (4), including the constraints enforced by the interactions satisfying Eq. (6).

It is essential in our scheme that we energetically isolate the stretched states $|n^2P_{3/2}, m = 3/2\rangle_{x,z}$ from the other m states in the given fine-structure manifold. This is necessary to protect these states from mixing with other Zeeman m levels. Such unwanted couplings can be induced by van der Waals interactions (see Sec. III B below) or via the light polarization of the Rydberg laser. This energetic protection requires an (effective) local magnetic field, which for the ● and ■ sites, points in the x and z directions, respectively. Strong local fields with spatial resolution on the scale given by the lattice spacing can be obtained via AC-Stark shifts, combining the m dependence of atomic AC tensor polarizabilities with spatially varying polarization gradients. Figure 4 outlines a scheme where we superimpose two
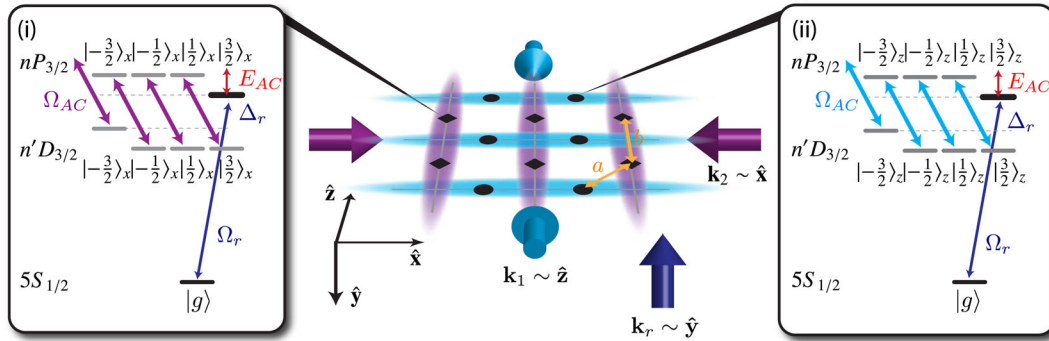

FIG. 4. We consider ^{87}Rb atoms loaded in a square optical lattice with lattice spacing a and lattice sites alternately labeled as ● and ■. Additional AC-Stark lasers (magenta and light-blue arrows) with wave vectors $\mathbf{k}_1 = \pm 2\pi/\lambda_{AC}\hat{\mathbf{z}}$ and $\mathbf{k}_2 = \pm 2\pi/\lambda_{AC}\hat{\mathbf{x}}$, respectively, form two pairs of standing waves, each with periodicity $b = \lambda_{AC}/2$, which are rotated by 45 degrees with respect to the initial lattice. In order to create local quantization axes along $\hat{\mathbf{z}}$ or $\hat{\mathbf{x}}$ for ● or ■ lattice sites, respectively, we require that atoms located on a ● lattice site only feel the intensity maxima of the light-blue laser with $\mathbf{k}_1 \sim \mathbf{z}$, while those located on a ■ lattice site only feel the intensity maxima of the magenta laser with $\mathbf{k}_2 \sim \hat{\mathbf{x}}$. This can be achieved by adjusting the initial trapping lattice by tilting the corresponding trapping lasers at an angle α such that $a = \lambda/[2\sin(\alpha/2)] \geq \lambda/2$ [73] in order to fulfill $b = \sqrt{2}a$. The two AC-Stark lasers have a polarization σ_+ and resonantly couple the $n^2P_{3/2}$ manifold to a lower-lying $n'D_{3/2}$ manifold, thereby inducing an AC-Stark shift on each Zeeman m level in the $n^2P_{3/2}$ manifold except for the maximum stretched $|n^2P_{3/2}, 3/2\rangle_{z,x}$ states. This locally isolates the $|n^2P_{3/2}, 3/2\rangle_z$ and $|n^2P_{3/2}, 3/2\rangle_x$ states at lattice sites ● and ■, respectively, in energy, by at least E_{AC} (see left and right panels). A global Rydberg laser (dark-blue arrow) with detuning $\Delta_r \ll E_{AC}$ propagating along the y direction then selectively admixes the states $|n^2P_{3/2}, 3/2\rangle_z$ and $|n^2P_{3/2}, 3/2\rangle_x$ at lattice sites ● and ■, respectively, to the ground state $|g\rangle$.

pairs of counterpropagating laser beams of wavelength λ_{AC} (light-blue and magenta arrows). They create a standing-wave pattern (light-blue and magenta gradients), such that ● lattice sites only see the intensity maxima of the standing wave propagating along the z direction (light-blue laser), while ■ lattice sites see the intensity maxima of the standing wave propagating along the x direction (magenta laser).

The AC-Stark lasers have polarization σ_+ and resonantly couple the $nP_{3/2}$ manifold to a lower-lying $n'D_{3/2}$ manifold (see magenta and blue arrows in the left and right panels of Fig. 4, respectively). This induces an AC-Stark shift on each Zeeman m level in the $n^2P_{3/2}$ manifold. The Rabi frequency is proportional to $\Omega_{AC} \sim \sqrt{(m - \frac{3}{2})(m + \frac{5}{2})}$ $\langle nP_{3/2}\|r\|n'D_{3/2}\rangle\mathcal{E}$, with $\mathcal{E}$ the electric-field strength of the AC-Stark lasers. In this configuration, the stretched states $|n^2P_{3/2}, m = 3/2\rangle_{z,x}$ of interest are not affected by the AC-Stark lasers. The minimum shift (as a function of $m \neq 3/2$) is denoted E_{AC}, which has to obey $E_{AC} \gg V_{\text{off}}$ and $E_{AC} \gg \Delta_r$ in order to suppress mixing between different m states due to van der Waals interactions and the excitation laser. Here, V_{off} is the largest off-diagonal van der Waals matrix element in the $n^2P_{3/2}$ manifold (see Appendix C).

The AC-Stark lasers will create an additional trapping potential, $V_{AC}(\mathbf{r}_i)|g\rangle\langle g|_i$, for ground-state atoms with minima that are not commensurate with the initial trapping lattice. In order not to distort the desired lattice structure, this additional potential must not be larger than the initial lattice potential (see Appendix A).

It is then possible to dress the ground-state atoms with either the $|r_\bullet\rangle = |n^2P_{3/2}, m = 3/2\rangle_z$ or the $|r_\blacksquare\rangle = |n^2P_{3/2}, m = 3/2\rangle_x$ Rydberg state by a single, global laser with Rabi frequency Ω_r and detuning Δ_r propagating in the direction perpendicular to the plane, i.e., $\mathbf{k}_r \sim \mathbf{y}$ (dark-blue arrow in Fig. 4). In the local x and z bases, this laser will couple to all four $|m\rangle_{z,x}$ levels with different weights (see Appendix B). Since the states $|m \neq 3/2\rangle_{z,x}$ are energetically separated by at least E_{AC} from the $|m = 3/2\rangle$ state, a laser with detuning $\Delta_r \ll E_{AC}$ and wave vector $\mathbf{k} \sim \mathbf{y}$ will selectively admix the states $|3/2\rangle_z$ and $|3/2\rangle_x$ at lattice sites ● and ■, respectively, to the ground state $|g\rangle$ with an effective Rabi frequency $\Omega'_r = \Omega_r/(2\sqrt{2})$. The single-particle Hamiltonian describing the laser dressing in a frame rotating with the laser frequency for an atom i then becomes

$$H_i = -\Delta_r |r_{\alpha_i}\rangle\langle r_{\alpha_i}|_i + \frac{1}{2}\Omega'_r(|g\rangle\langle r_{\alpha_i}|_i + |r_{\alpha_i}\rangle\langle g|_i), \quad (7)$$

where $\alpha_i \in \{\bullet, \blacksquare\}$ depends on the lattice site of the ith atom. In the weakly dressing regime, $\Delta_r \gg \Omega_r$, the new dressed ground states are $|\bullet\rangle_i \equiv |g\rangle_i + \Omega_r/(2\Delta_r)|r_\bullet\rangle_i$ or $|\blacksquare\rangle_i \equiv |g\rangle_i + \Omega_r/(2\Delta_r)|r_\blacksquare\rangle_i$ if $\alpha_i = \bullet$ or $\blacksquare$, respectively.

Thus, each ground-state atom gets a small admixture of one of the Rydberg states, depending on the sublattice. Because of the weak admixture of the Rydberg states, the dressed ground states get a comparatively small decay rate $\tilde{\Gamma} = (\Omega_r/2\Delta_r)^2\Gamma$, where Γ is the decay rate of the bare Rydberg state, which has to be much smaller than the relevant system's energy scales discussed below.

B. Interactions between p states

We consider the van der Waals interactions, $V_{\bullet\bullet}$, $V_{\bullet\blacksquare}$, and $V_{\blacksquare\blacksquare}$, between pairs of atoms prepared in the bare Rydberg states $|r_\bullet\rangle = |n^2P_{3/2}, m = 3/2\rangle_z$ and $|r_\blacksquare\rangle = |n^2P_{3/2}, m = 3/2\rangle_x$. For Rubidium atoms excited to Rydberg p states, these van der Waals forces are strongly anisotropic [52–55]. Figure 5(a) shows the angular part of the van der Waals interaction, $V_{\bullet\bullet}$, for different n values, which is a very good approximation proportional to

$$V_{\bullet\bullet}(r, \vartheta) \sim \frac{(ea_0)^4 n^{11}}{r^6}\sin^4\vartheta, \quad (8)$$

while the actual strength depends on the principal quantum number n and scales as n^{11} away from the Förster resonance at $n = 38$. A detailed discussion of this scaling behavior and of the resonance origin can be found in Ref. [54]. Similarly, one finds for the interaction between $|r_\blacksquare\rangle = |n^2P_{3/2}, m = 3/2\rangle_x$ Rydberg states,

$$V_{\blacksquare\blacksquare}(r, \vartheta) \sim \frac{(ea_0)^4 n^{11}}{r^6}\cos^4\vartheta, \quad (9)$$

which can be obtained by rotating the coordinate system by $\pi/2$. Mixed interactions such as

$$V_{\bullet\blacksquare}(r, \vartheta) \sim \frac{(ea_0)^4 n^{11}}{r^6}(3\sin 2\vartheta + 2)^2 \quad (10)$$

are shown in Fig. 16 (Appendix D) and have two asymmetric maxima at $\vartheta = \pm\pi/4$. The Rydberg states $|r_\bullet\rangle$ and $|r_\blacksquare\rangle$ therefore realize the desired angular interaction properties, as discussed in Sec. II B. Together with the possibility of creating soft-core potentials (see the following subsection), the anisotropy of these interactions naturally leads to the desired interaction pattern illustrated in Fig. 1(b) and demanded by Eq. (6). These interactions underly our realization of the Bose-Hubbard Hamiltonian (4).

We now detail the physical mechanism that generates these anisotropic interactions, and we describe how to derive the aforementioned results. Van der Waals interactions between two atoms i and j prepared in a given Rydberg state arise from the exchange of virtual photons: Atom i in a Rydberg state $|r_i\rangle$ can, for example, virtually undergo a dipole-allowed transition to a lower-lying electronic state $|\alpha\rangle$ while emitting a photon. If this virtual
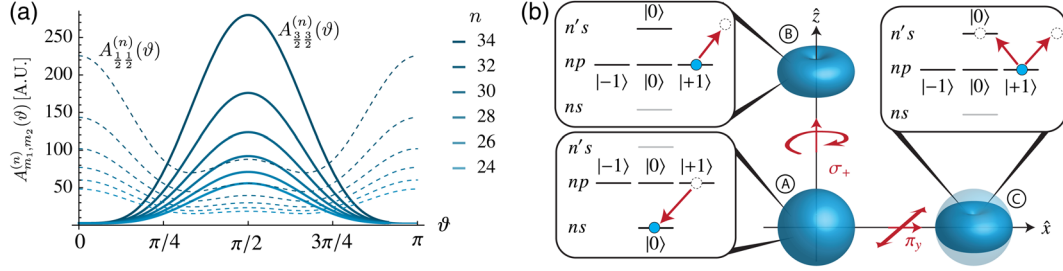
FIG. 5. (a) Angular part, $A^{(n)}_{m_1,m_2}(\vartheta)$, of the van der Waals interaction, $V^{(n)}_{m_1,m_2}(r,\vartheta) = \langle m_1,m_2|\hat{V}_{\mathrm{vdW}}|m_1,m_2\rangle = (n-\delta_{n\ell j})^{11}A^{(n)}_{m_1,m_2}(\vartheta)/r^6$, between a pair of ^{87}Rb atoms in the $|3/2,3/2\rangle_z \equiv |n^2P_{3/2},3/2\rangle_z \otimes |n^2P_{3/2},3/2\rangle_z$ state (solid lines) and in the $|1/2,1/2\rangle_z \equiv |n^2P_{3/2},1/2\rangle_z \otimes |n^2P_{3/2},1/2\rangle_z$ state (dashed lines). We plot the angular part of the rescaled interaction energy, $A^{(n)}_{m_1,m_2}$, as a function of the angle ϑ for various values of the principal quantum number n in atomic units. Here, $A^{(n)}_{3/2,3/2}$ (solid lines) corresponds to the angular part of the interaction, $V_{\bullet\bullet}$, between two atoms excited to the $|r_\bullet\rangle$ Rydberg state, and it shows a characteristic $\sim \sin^4\vartheta$ shape due to the dominant $S_{1/2}$ channel. Residual interactions at $\vartheta = 0$ are very small and arise from channels coupling to virtual D states (see Table I). (b) The angular characteristic of the interaction between two atoms, both in the "stretched" Rydberg state, $|r_\bullet\rangle = |n^2P_{3/2},3/2\rangle_z = |np,1\rangle_z|\frac{1}{2}\frac{1}{2}\rangle_z$, can be qualitatively understood from its angular part $|np,1\rangle_z$ and the dominating S channel: Atom A prepared in a $|np,1\rangle_z$ state can make a virtual transition to a lower-lying $|ns,0\rangle_z$ state (red arrow in the lower left panel) while emitting a photon. If this photon propagates along the z direction, it has polarization σ_+ and cannot be absorbed by atom B. Therefore, atom A and atom B will not interact, i.e., $V_{\bullet\bullet}(\vartheta = 0) = 0$. If this photon propagates along the x direction, it is linearly polarized with a polarization vector along the y direction. In the frame of atom C, this photon will drive both σ_+ and σ_- transitions and thus can be absorbed. Hence, atom A can interact with atom C, i.e., $V_{\bullet\bullet}(\vartheta = \pi/2) \neq 0$.

photon reaches atom j during its lifetime, it can excite the second atom to an electronic state $|\beta\rangle$. This then leads to correlated oscillations of instantaneously induced dipoles in both atoms, which give rise to the nonretarded van der Waals force [74]. For the familiar case of s states, these interactions are isotropic, $V_{\mathrm{VdW}}(r) = C_6/r^6$, with the van der Waals coefficient C_6 scaling as $C_6 \sim n^{11}$ [52–55]. Here, n is the principal quantum number and r the distance between atoms. These van der Waals interactions between Rydberg states exceed ground-state interactions by several orders of magnitude and have been observed and explored in recent experiments [23–37].

In the case of Rydberg p states, the angular distribution of these emission and absorption processes of virtual photons, in combination with the angular momentum structure of the atomic orbitals, leads to nontrivial anisotropic van der Waals interactions [52–55]. We now focus on the van der Waals interaction $V_{\bullet\bullet}$ between both atoms in the $|r_\bullet\rangle = |n^2P_{3/2}, m = 3/2\rangle_z$ Rydberg state with the quantization axis along the z direction. Mixed interactions $V_{\bullet\blacksquare}$ and interactions between both atoms in the $|r_\blacksquare\rangle = |n^2P_{3/2}, m = 3/2\rangle_x$ Rydberg state, $V_{\blacksquare\blacksquare}$, will be derived in Appendix C. The latter can simply be obtained by rotating the xz plane by 90 degrees, i.e., $V_{\blacksquare\blacksquare}(r,\vartheta) = V_{\bullet\bullet}(r,\vartheta - \pi/2)$, while in order to calculate mixed interactions, one has to calculate off-diagonal matrix elements in the $n^2P_{3/2}$ manifold.

In general, van der Waals interactions arise as a second-order process from the dipole-dipole interaction $\hat{V}^{(ij)}_{\mathrm{dd}}(\mathbf{r}) = (\mathbf{d}^{(i)} \cdot \mathbf{d}^{(j)} - 3(\mathbf{d}^{(i)} \cdot \mathbf{n})(\mathbf{d}^{(j)} \cdot \mathbf{n}))/r^3$, where V_{dd} couples the initial Rydberg states $|r_i, r_j\rangle$ to virtual intermediate

states $|\alpha, \beta\rangle$ and back. Here, $\mathbf{d}^{(i)}$ is the dipole operator of the ith atom, and $\mathbf{r} = r\mathbf{n} = (r,\vartheta,\varphi)$ is the relative distance between atom i and atom j, with $\mathbf{n}$ a unit vector and (r,ϑ,φ) the spherical coordinates. It is convenient to rewrite the latter expression in a spherical basis [75]

$$\hat{V}^{(ij)}_{\mathrm{dd}}(\mathbf{r}) = -\sqrt{\frac{24\pi}{5}}\frac{1}{r^3}\sum_{\mu,\nu} C^{1,1;2}_{\mu,\nu;\mu+\nu} Y_2^{\mu+\nu}(\vartheta,\varphi)^* d^{(i)}_\mu d^{(j)}_\nu,$$

(11)

with $d^{(i)}_\mu$ the spherical components ($\mu,\nu \in \{-1,0,1\}$) of $\mathbf{d}^{(i)}$, $C^{j_1,j_2;J}_{m_1,m_2;M}$ the Clebsch-Gordan coefficients, and Y_l^m the spherical harmonics.

Because of the dipole selection rules, states in the $n^2P_{3/2}$ manifold can only couple to states in a $n'S_{1/2}$, $n'D_{5/2}$ or $n'D_{3/2}$ manifold. It turns out that for ^{87}Rb, the dominating channel is $P_{3/2} + P_{3/2} \longrightarrow S_{1/2} + S_{1/2}$, which can be explicitly seen from Table I for various n levels. In order to simplify the following discussion, we will first focus on this channel and neglect all other channels, including $D_{3/2}$ and $D_{5/2}$ states which lead to small imperfections, as discussed in Appendix C.

For a single atom, the $|n^2P_{3/2}, \frac{3}{2}\rangle$ state is a stretched state that reads, in the uncoupled basis, $|n^2P_{3/2}, \frac{3}{2}\rangle \equiv |np,1\rangle \otimes |\frac{1}{2},\frac{1}{2}\rangle$. Thus, it can be factorized into an angular and a spin degree of freedom. Since the dipole-dipole interaction $\hat{V}_{\mathrm{dd}}(\mathbf{r})$ does not couple spin degrees of freedom, the angular dependence of the van der Waals interaction is

TABLE I.　Two atoms, both in the $|r_\bullet\rangle = |n^2P_{3/2}, 3/2\rangle_z = |np, 1\rangle_z |\frac{1}{2}\frac{1}{2}\rangle_z$ state, can couple to six channels. Each channel ν has a characteristic angular dependency $(\mathcal{D}_\nu)_{\frac{33}{22}}$ that contributes with weight $C_6^{(\nu)}$. The total interaction can be obtained by summing over all channels, i.e., $V_{\bullet\bullet}(r, \vartheta) = 2\sum_\nu C_6^{(\nu)} \langle\frac{3}{2}\frac{3}{2}|\mathcal{D}_\nu(\vartheta)|\frac{3}{2}\frac{3}{2}\rangle/r^6$. It turns out that two atoms in the $|r_\bullet\rangle$ Rydberg state dominantly couple to the $S_{1/2} + S_{1/2}$ channel with a characteristic angular dependence $\sim \sin^4 \vartheta$.

	$C_6^{(\nu)}$ (A.U.)					
Channel ν	$n = 26$	$n = 28$	$n = 30$	$n = 32$	$n = 34$	$\langle\frac{3}{2}\frac{3}{2}|\mathcal{D}_\nu(\vartheta)|\frac{3}{2}\frac{3}{2}\rangle$
$S_{1/2} + S_{1/2}$	1.58×10^{17}	5.07×10^{17}	1.60×10^{18}	4.88×10^{18}	1.61×10^{19}	$\sin^4 \vartheta/4$
$S_{1/2} + D_{3/2}$	6.38×10^{15}	1.60×10^{16}	3.72×10^{16}	8.15×10^{16}	1.70×10^{17}	$(2 + \cos 2\vartheta) \sin^2 \vartheta/50$
$S_{1/2} + D_{5/2}$	6.46×10^{15}	1.62×10^{16}	3.76×10^{16}	8.26×10^{16}	1.72×10^{17}	$(209 + 84 \cos 2\vartheta + 27 \cos 4\vartheta)/2400$
$D_{3/2} + D_{3/2}$	-1.17×10^{15}	-2.71×10^{15}	-5.85×10^{15}	-1.20×10^{16}	-2.34×10^{16}	$(5 + 2 \cos 2\vartheta + \cos 4\vartheta)/1250$
$D_{3/2} + D_{5/2}$	-1.06×10^{15}	-2.43×10^{15}	-5.20×10^{15}	-1.06×10^{16}	-2.05×10^{16}	$(358 + 186 \cos 2\vartheta - 27 \cos 4\vartheta)/15000$
$D_{5/2} + D_{5/2}$	-9.50×10^{14}	-2.15×10^{15}	-4.56×10^{15}	-9.16×10^{15}	-1.76×10^{16}	$3(1745 - 876 \cos 2\vartheta + 27 \cos 4\vartheta)/20000$

determined solely by the angular part of the wave function, which is $|np, 1\rangle$.

Figure 5(b) illustrates the interaction between two atoms initially prepared in a $|np, 1\rangle$ state as a function of ϑ for $\vartheta = 0$ (atoms A and B) and $\vartheta = \pi/2$ (atoms A and C). We first consider atom A in the lower left corner of Fig. 5(b). Initially prepared in a $|np, 1\rangle$ state, it can make a virtual transition to a lower-lying $|ns, 0\rangle$ state [red arrow in the lower left panel of Fig. 5(b)] while emitting a photon. The corresponding angular distribution of the spontaneously emitted photon has the same characteristic as light emitted by a classical dipole tracing out a circular trajectory in the x-y plane [75]. In general, it is elliptically polarized with cylindrical symmetry, but in particular, there are two specific directions: (i) Light emitted along the z direction ($\vartheta = 0$) is circularly polarized, rotating in the same way as the dipole. Thus, a photon emitted in the z direction has polarization σ_+ and carries one unit of angular momentum such that the total angular momentum of the combined atom-photon system is conserved. A second atom, labeled as atom B in Fig. 5(b), located on the z axis ($\vartheta = 0$), cannot absorb this photon [see red arrow in the upper left panel of Fig. 5(b)] since only a $|n's, 0\rangle$ state is available. The same result can be derived from Eq. (11), which for $\vartheta = 0$ simplifies to

$$\hat{V}_{dd}^{(ij)}(\vartheta = 0) = -\frac{2}{r^3} \sum_\mu \frac{d_\mu^{(i)} d_{-\mu}^{(j)}}{(1 - \mu)!(1 + \mu)!} \qquad (12)$$

and couples only states with initial magnetic quantum number m_1, m_2 to states with $m_1 \pm 1$, $m_2 \mp 1$, such that the total angular momentum $M = m_1 + m_2$ is conserved. Therefore, the dipole-dipole matrix element vanishes, $\langle np1, np1|\hat{V}_{dd}^{(AB)}(\vartheta = 0)|ns0, n's0\rangle = 0$, and hence, atoms A and B do not interact. (ii) Light emitted into the x-y plane ($\vartheta = \pi/2$) is linearly polarized, with a polarization vector lying in the x-y plane and perpendicular to the emission direction. A third atom, labeled as atom C in Fig. 5(b), located on the x axis is able to absorb this linearly polarized

photon emitted by atom A, which in the frame of atom C corresponds to a superposition of σ_+ and σ_- polarized light [see red arrows in the right panel of Fig. 5(b)]. For $\vartheta = \pi/2$, Eq. (11) contains a sum over $\cos[(\pi/2)(\mu + \nu)]$, and the only nonvanishing combinations for $\mu = -1$ are $\nu = \pm 1$. Thus, the dipole matrix element $\langle np1, np1|\hat{V}_{dd}^{(AC)}(\vartheta = \pi/2)|ns0, n's0\rangle$ is nonzero, and atoms A and C will interact.

In general, for the dominant channel $P_{3/2} + P_{3/2} \longrightarrow S_{1/2} + S_{1/2}$, only the term $d_{-1}^{(1)} d_{-1}^{(2)}$ with $\mu = \nu = -1$ in Eq. (11) can contribute to the dipole-dipole matrix element, and thus, the van der Waals interaction between both atoms in a $n^2P_{3/2}, m = 3/2$ states becomes $V_{\frac{3}{2}\frac{3}{2}}^{(n)}(r, \vartheta, \varphi) \sim (Y_2^{-2})^2 \sim \sin^4 \vartheta$ for this channel. Residual interactions at $\vartheta = 0$ and π come from couplings to $D_{3/2,5/2}$ channels which are small (see Table I). Thus, using Rubidium $n^2P_{3/2}$ states with $m_j = 3/2$ allows an almost perfect realization of an anisotropic interaction with a vanishing interaction along one axis and a large interaction along a perpendicular axis. Note that interactions between two atoms in $|n^2P_{3/2}, m = 3/2\rangle$ are negative (attractive) for $n > 38$ and positive (repulsive) for $n < 38$, where a Förster resonance at $38P_{3/2} + 38P_{3/2} \longrightarrow 38S_{1/2} + 39S_{1/2}$ changes the sign of the interaction [52–55]. Figure 5(a) shows the result of the full calculation of the van der Waals interactions between $n^2P_{3/2}, 3/2$ states including all channels and summing over n' and n'' levels between $n \pm 10$. The full calculation agrees well with the simplified picture discussed above and illustrated in Fig. 5(b) since the dominating channel is the one coupling to $S_{1/2}$ states. Moreover, it is in full agreement with previous studies on anisotropic interactions between Rb Rydberg states [54].

C. Soft-core potentials

In the previous section, we showed how to engineer the anisotropic part of the interactions required by Eq. (6). We now briefly review how to create soft-core potentials by
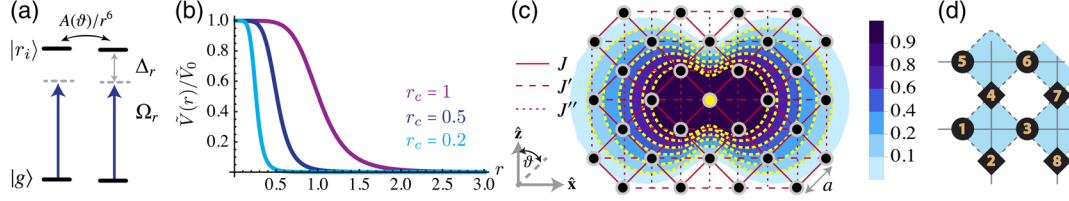
FIG. 6. (a) Qualitative sketch of the energy levels (black lines) and lasers (thick solid dark-blue arrows) required for the Rydberg dressing scheme. The ground state $|g\rangle$ of each atom is off-resonantly coupled to a Rydberg state $|r_i\rangle$ with a continuous wave laser of Rabi frequency Ω_r and detuning Δ_r (see also Fig. 4). Pairwise interactions between the energetically well-isolated Rydberg states can be anisotropic, i.e., $V_{ij}(\mathbf{r}) = A(\vartheta)/r^6$. (b) Energy eigenvalues $\tilde{V}(\mathbf{r})$ of Eq. (14) (dressed Born-Oppenheimer potential surfaces) of Rydberg-dressed ground-state atoms for different values of the Condon radius r_c defined in Eq. (15). The potential has a steplike shape and saturates for small distances at $\tilde{V}_0$, while the onset of the steep slope is given by r_c. (c) Contour plot of the dressed ground-state interaction $\tilde{V}_{ij}(\mathbf{r})/\tilde{V}_0$ between the atom in the middle (yellow circle) and the surrounding atoms (black circles) arranged on a square lattice, all in the $|r_\bullet\rangle$ Rydberg state. In this case, $A(\vartheta) \sim \sin^4\vartheta$, which gives rise to a figure-eight-shaped interaction plateau (yellow dashed lines). Residual interactions along $\vartheta = 0$ come from virtual transitions to D states (see Sec. III B). (d) Labeling of the lattice sites for the example of Sec. III D.

weakly admixing the Rydberg states to the atomic ground state [56,59]. This guarantees that interactions between atoms sitting on a square lattice at different distances a and $\sqrt{2}a$ experience the same interaction potential [76], as required by Eq. (6) and illustrated in Fig. 1(b).

The single-atom configuration we have in mind was introduced in Sec. III A and is governed by the Hamiltonian of Eq. (7). Pairwise interactions [see Fig. 6(a)] between N atoms, both excited to the Rydberg states $|r_i\rangle|r_j\rangle$, are described by

$$H_{ij}(\mathbf{r}_{ij}) = V_{ij}(\mathbf{r})|r_i\rangle\langle r_i| \otimes |r_j\rangle\langle r_j|, \qquad (13)$$

where $V_{ij}(\mathbf{r}_{ij}) = A_{ij}(\vartheta_{ij},\varphi_{ij})/r_{ij}^6$ is the van der Waals interaction potential between the Rydberg states of atom i and atom j discussed in the previous section and $(r_{ij},\vartheta_{ij},\varphi_{ij})$ are the spherical coordinates of the relative vector.

Following the s-state case [57–60], Brillouin-Wigner perturbation theory up to fourth order in the small parameter $\Omega_r/(2\Delta_r) \ll 1$ results in a sum of binary interactions between the dressed ground state atoms of the form

$$\tilde{V}_{ij} = 2\Delta_r\left(\frac{\Omega_r}{2\Delta_r}\right)^4 \frac{r_c^6(\vartheta_{ij},\varphi_{ij})}{r_c^6(\vartheta_{ij},\varphi_{ij}) + r_{ij}^6}, \qquad (14)$$

with

$$r_c(\vartheta_{ij},\varphi_{ij}) = \left(\frac{A_{ij}(\vartheta_{ij},\varphi_{ij})}{2|\Delta_r|}\right)^{1/6} \qquad (15)$$

being the Condon radius. In the case of p-Rydberg states, where the interactions are *anisotropic*, the Condon radius depends on the angular pattern of the van der Waals interaction $A(\vartheta,\varphi)$, which can be tuned by choosing a particular Rydberg state. Additionally, the Condon radius can be scaled by changing the detuning Δ_r of the dressing laser. Figure 6(b) shows typical examples of the dressed ground-state potential $\tilde{V}_{ij}$ for red detuning $\Delta_r < 0$ and

repulsive interactions $V_{ij} > 0$, for different Condon radii r_c. For large distances, $r \gg r_c$, the dressed ground-state potential is proportional to the Rydberg interaction, $\tilde{V}_{ij} = \Omega_r^4/(2\Delta_r)^4 V_{ij} \sim 1/r_{ij}^6$, reduced by a factor $[\Omega_r/(2\Delta_r)]^4$ arising from the small probability to excite both atoms to the Rydberg state. However, for small distances, $r < r_c$, when two atoms are within the Condon radius, the excitation to the Rydberg states becomes ineffective because of the large total detuning $|\Delta_r| + V_{ij}$ (dipole blockade), and the effective ground-state interaction, $\tilde{V}_{ij} \approx \tilde{V}_0[1 - (r/r_c)^6]$ for $r < r_c$, saturates at a constant value $\tilde{V}_0 = \Omega_r^4/(2\Delta_r)^3$, which is independent of the strength or form of the Rydberg-Rydberg interactions. The presence of a plateau at short distances $r < r_c$ and a rapid decrease of the potential at $r \sim r_c$, where $\tilde{V}_{ij} \sim 1/r_{ij}^6$, allows us to engineer approximately equal interactions between atoms within r_c independent of their specific distance. At the same time, long-range interactions, between, e.g., next-nearest-neighbors (NNN), are substantially suppressed.

Combining the steplike ground-state potentials of Eq. (14) with anisotropic interactions discussed in the previous section leads to figure-eight-shaped plateau potentials shown in Fig. 6(c). Here, atoms (black circles) interact with J, J', and J'' along the ± 45-degree lines, the x axis and the z axis, respectively, with the atom in the middle (yellow circle). It is possible to tune the interaction strength J, J', and J'' over a large range by, e.g., changing the detuning Δ_r or the principal quantum number n of the Rydberg state. In particular, one can realize an interaction pattern where atoms sitting at different distances, a and $\sqrt{2}a$, interact with equal strength, that is, $J \approx J'$, while $J'' \ll J$, thus realizing a frustrated $J - J'$ model. Note that the interaction symmetry in this case is triangular on top of a square lattice.

D. Explicit numbers and discussion of imperfections

As an explicit example, we consider the $29^2P_{3/2}$ Rydberg manifold of ^{87}Rb. We resonantly couple the $29^2P_{3/2}$ manifold to the lower-lying $7^2D_{3/2}$ manifold, as

illustrated in Fig. 4 ($n = 29$ and $n' = 7$), with a laser of wavelength $\lambda_{AC} = 3.296\,\mu m$. This results in a lattice spacing $a = \lambda_{AC}/(2\sqrt{2}) = 1.16\,\mu m$, which can be adjusted by tilting the trapping lasers by an angle $\alpha = 39$ degrees (see Sec. III A).

For the van der Waals interactions between the Rydberg states $|r_\bullet\rangle = |29^2 P_{3/2}, 3/2\rangle_z$ and $|r_\blacksquare\rangle = |29^2 P_{3/2}, 3/2\rangle_x$, we find

$$V_{\bullet\bullet}(r, \vartheta) = 2\pi \times \frac{25.4 - 31.9\cos 2\vartheta + 8.2\cos 4\vartheta}{(r/\mu m)^6}\,\text{MHz},$$

$$V_{\blacksquare\blacksquare}(r, \vartheta) = 2\pi \times \frac{25.4 + 31.9\cos 2\vartheta + 8.2\cos 4\vartheta}{(r/\mu m)^6}\,\text{MHz},$$

$$V_{\bullet\blacksquare}(r, \vartheta) = 2\pi \times \frac{16.8 - 8.2\cos 4\vartheta + 20.3\sin 2\vartheta}{(r/\mu m)^6}\,\text{MHz},$$

$$(16)$$

including all channels of Table I and summing over $\pm 10\,n$ values (see Appendixes C and D). They are plotted in Figs. 5(a) and 16. The largest off-diagonal matrix element coupling different Zeeman m levels is $V_{\text{off}}(a) = \langle \frac{3}{2}\frac{3}{2}|\hat{V}_{\text{vdW}}(a, \pi/2)|\frac{1}{2}\frac{1}{2}\rangle = 2\pi \times 11.2\,\text{MHz}$. Using an AC-Stark laser with power $P = 1.0\,\text{mW}$ focused on an area $A = 50\,\mu m^2$ yields a Rabi frequency $\Omega_{AC} = 2d_{7D-29P} \mathcal{E}_{AC}/\hbar = 2\pi \times 205.5\,\text{MHz}$, where $d_{7D-29P} = \langle 7D_{3/2}, 3/2|d|29P_{3/2}, 1/2\rangle = 0.065\,ea_0$ is the smallest transition dipole moment and $\mathcal{E}_{AC} = \sqrt{2P/c\epsilon_0 A}$ is the electric-field strength. The AC-Stark lasers will create an additional ground-state potential with depth $V_{AC} = 2\pi \times 27.8\,\text{kHz}$; thus, the initial trapping potential V_{trap} must be larger than V_{AC} (see Appendix A).

Adjusting the detuning Δ_r of the Rydberg laser allows us to tune the length scale and the imperfections in Eq. (14). These are as follows: (i) small long-range interactions between nearest-neighbor lattice sites and (ii) deviations from the constraint model of Eq. (6). Here, for example, we use $\Delta_r = 2\pi \times 400\,\text{kHz}$, which yields the following interaction pattern between particles labeled in Fig. 6(d): $\tilde{V}_{14}/\tilde{V}_0 = \tilde{V}_{23}/\tilde{V}_0 = 0.96$, $\tilde{V}_{13}/\tilde{V}_0 = \tilde{V}_{24}/\tilde{V}_0 = 0.80$, $\tilde{V}_{12}/\tilde{V}_0 = \tilde{V}_{34}/\tilde{V}_0 = 0.70$ around a vertex and small imperfect interactions between different vertices, e.g., $\tilde{V}_{15}/\tilde{V}_0 = \tilde{V}_{28}/\tilde{V}_0 = 0.09$, and next-nearest-neighbor interactions, e.g., $\tilde{V}_{16}/\tilde{V}_0 = \tilde{V}_{27}/\tilde{V}_0 = 0.12$ or $\tilde{V}_{18}/\tilde{V}_0 = \tilde{V}_{25}/\tilde{V}_0 = 0.01$.

By varying the Rabi frequency of the Rydberg laser $\Omega_r = 2\pi \times (120, 160, 200)\,\text{kHz}$, one obtains $\epsilon = \Omega_r/2\Delta_r = (0.15, 0.20, 0.25)$, which gives rise to an effective ground-state interaction $\tilde{V}_0 = \Omega_r^4/8\Delta_r^3 = 2\pi \times (405, 1280, 3125)\,\text{Hz}$. This is much larger than the effective decay rate from the dressed ground state $\tilde{\Gamma} = \epsilon^2\Gamma = 2\pi \times (74, 132, 206)\,\text{Hz}$, and larger than a corresponding tunneling rate between the minima. Here, $\Gamma = 2\pi \times 3.3\,\text{kHz}$ is the decay rate from the Rydberg states.

There is ample choice in the parameter regimes available as a function of the n level. Away from the Förster
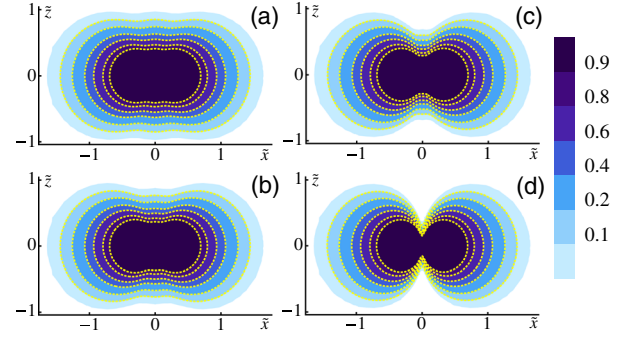

FIG. 7. Soft-core potentials (in units of $\tilde{V}_0$) of Eq. (14) between $n^2 P_{3/2}$, $m_j = 3/2$ Rydberg states with (a) $n = 25$, $A((\pi/2), 0) = 2\pi \times 6.3\,\text{MHz}\,\mu m^6$ (b) $n = 30$, $A((\pi/2), 0) = 2\pi \times 114.8\,\text{MHz}\,\mu m^6$, (c) $n = 36$, $A((\pi/2), 0) = 2\pi \times 4.8\,\text{GHz}\,\mu m^6$, and (d) $n = 38$, $A((\pi/2), 0) = 2\pi \times 390.0\,\text{GHz}\mu m^6$. Here, $\tilde{x} = x/r_c((\pi/2), 0)$ and $\tilde{z} = z/r_c((\pi/2), 0)$ are dimensionless, with r_c defined in Eq. (15). Residual interactions along the z direction come from virtual transitions to D channels and depend on the principal quantum number n (see Table I).

resonance at $n = 38$, it is possible to engineer infrared lattices that allow for comparable time scales between the interactions induced by the dressing and the tunneling matrix elements of the atoms on the original square lattice. Going higher in n, closer to the Förster resonance, allows for faster time scales and slower decays; however, in this case, the infrared laser has a strong influence on the underlying lattice, excluding the possibility of using conventional single-particle tunneling to induce quantum fluctuations. On the other hand, one can profit here from the richness of the Rydberg manifolds involved, realizing the hopping matrix element as a spin-exchange coupling between different atoms sitting at different potential minima [77]. In both cases above, the interaction pattern will depend on the specific targeted n, as discussed in Sec. III B. As the qualitative (and in many respects, quantitative, as indicated in Table I and Fig. 7) shape of the interactions will be very similar in the interval of interest $n = 25$–37, we will focus, in the following, on a single-case sample to underpin the stability of the many-body effects in which we are interested.

IV. NUMERICAL RESULTS

In this section, we consider the properties of the approximate realization of the quantum spin-ice model Hamiltonian proposed above. We demonstrate that, as a function of the strength of the quantum dynamics, the ground state has two regimes reflecting two distinct forms of ordering (Sec. IV B). One, stabilized via a quantum order-by-disorder mechanism, generates the above-mentioned plaquette phase for sufficiently strong quantum dynamics. As it is weakened, there is a transition into a phase with classical ordering, which is stabilized by

the long-range parts of the dipolar couplings and which breaks translational symmetry in a different way. In addition, we show that even without quantum dynamics, there is an interesting thermal phase transition to an approximate realization of a (classical) Coulomb phase, with only a very small density of defects (plaquettes violating the ice rule) of around 5% (Sec. IV C 2). We discuss signatures of these items in various quantities, in particular, proposing a simple correlation function in which the quantum plaquette order will be visible, and which should be accessible in cold-atom experiments via *in situ* parity measurements [33,78,79].

A. General definitions and conventions

We begin with some general definitions and technical details of our numerical study. We consider both the unconstrained spin-1/2 model H from Eq. (5) and the projected model H_2 inside the spin-ice manifold:

$$H = \sum_{i<j} J_{ij} S_i^z S_j^z + J_\perp \sum_{\langle ij \rangle} (S_i^+ S_j^- + S_i^- S_j^+)$$

$$H_2 = \sum_{i<j} J_{ij} S_i^z S_j^z - t \sum_{\substack{j \square k \\ i \square l}} (S_i^+ S_j^- S_k^+ S_l^- + \text{H.c.}).$$

Here, $\langle ij \rangle$ denote nearest-neighbor (NN) sites on the 2D checkerboard lattice, and $(ijkl)$ label, clockwise, the four sites around empty square plaquettes. Note that only the empty plaquettes with alternating up-down spins (or "flippable" plaquettes) contribute to the second term of H_2. In our exact diagonalizations (ED), we have considered finite-size clusters with periodic boundary conditions and $N = 16$, 32, 36, 64, and 72 sites (see details in

Appendix E). To treat these clusters with ED, we exploit translational symmetry and point-group operations (the model has C_{2v} symmetry), as well as spin inversion ($S_z \to -S_z$) inside the total magnetization sector $S_z = 0$. Consequently, the eigenstates are labeled by linear momentum **k**, the irreducible representations of the point group of **k**, and the parity under spin inversion.

We note that, whereas the quantum phase is quite robust, the classical phase is considerably less so, reflecting the many nearly degenerate classical ice states. We illustrate this in Appendix F by imposing a variable cutoff on the long-range aspect of the dipolar couplings J_{ij}: By neglecting terms weaker than a cutoff J_c, we find a set of states with different classical orders, which settle down into the correct ground state without truncation for J_c no larger than 0.001.

B. The two zero-temperature phases: Low-energy spectroscopy and ground-state diagnostics

Figure 8 shows the low-energy spectra of H as a function of $J_\perp$ for $N = 32$ (a) and $N = 36$ (b), and that of H_2 as a function of t for $N = 64$ (c). All spectra correspond to the total magnetization sector $S_z = 0$ and a cutoff value of $J_c = 0.001$. In all spectra, there is a manifold of low-lying states that is well separated from higher-energy excitations. Provided they become degenerate in the thermodynamic limit, these states are the finite-size fingerprints of the spontaneously symmetry-broken phases [80–84]: Their multiplicities and symmetry content reveal the nature of the ground state (GS). The structure of the low-lying energy states consistently shows two qualitatively different phases. One is adiabatically connected to the classical limit $J_\perp = 0$, and the other is stabilized for large enough $J_\perp$ or t.
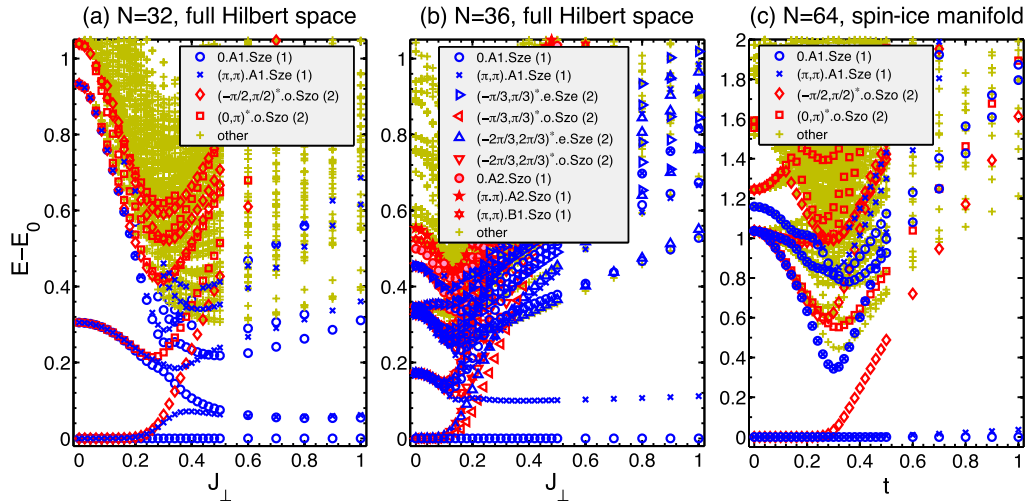

FIG. 8. (a,b) Low-energy spectra of H (in units of $\tilde{V}_0$) versus $J_\perp$ for N = 32 (a) and 36 (b), in the total magnetization sector $S_z = 0$ and for the cutoff $J_c = 0.001$. (c) Low-energy spectra of the constrained, spin-ice model H_2 versus t for 64 sites. The eigenstates are labeled by linear momentum **k**, the irreducible representations of the point group of **k** (the point group of the model is C_{2v}), and parity under spin inversion ("Sze" and "Szo" stand for even and odd parity, respectively). Numbers inside parentheses give the multiplicity of each energy level.

Classical phase: spin–spin correlations   Plaquette phase: energy correlations

(a) N=32, full Hilbert space, $J_\perp$=0.1 (b) N=64, spin–ice manifold, t=0.1   (c) N=64, spin–ice manifold, t=1
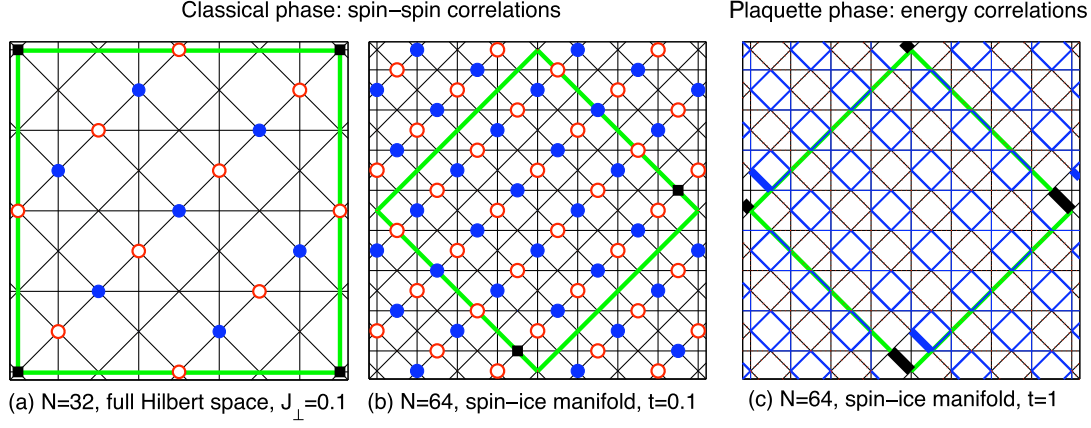
FIG. 9.   Ground-state diagnostics of the classical (a,b) and the QM plaquette (c) phases: Spin-spin correlation profiles (of the type $\langle S_i^z S_j^z \rangle$, where i is the reference site, indicated by a filled black square) in the ground state of (a) H for $N = 32$ and $J_\perp = 0.1$, and (b) H_2 for $N = 64$ and $t = 0.1$. Filled blue (open red) circles correspond to positive (negative) amplitude. (c) Connected energy correlation profiles [of the type $\langle S_i^z S_j^z S_k^z S_l^z \rangle - \langle S_i^z S_j^z \rangle \langle S_k^z S_l^z \rangle$, where the reference bond (ij) is indicated by the thick black segment] in the ground state of H_2 for $N = 64$ and $t = 1$. Solid blue (dashed red) bonds indicate positive (negative) amplitudes, while the width of each bond scales with the magnitude. All data correspond to the symmetry sector "0.A1.Sze" and are taken for the cutoff $J_c = 0.001$.

We begin with the classical phase, focusing on the $N = 32$ (a) and $N = 64$ (c) results first. Here, we find four low-lying states that become exactly degenerate as $J_\perp \to 0$. We find translational symmetry breaking with ordering wave vector $\mathbf{Q} = (-\pi/2, \pi/2)$, as illustrated in Fig. 3(c). The nature of this phase is revealed by the spin-spin correlation profiles of Figs. 9(a) and 9(b), with alternating up-down spins along one of the two diagonal directions of the lattice. The vanishing of correlations on every second diagonal line arises because of the existence of two states that are compatible with the nonvanishing correlations on the other diagonals. For a finite cluster, these appear with equal weight and thus average out, while in the thermodynamic limit, symmetry breaking spontaneously selects one of the two. Finally, the $N = 36$ cluster cannot accommodate the $\mathbf{Q} = (-\pi/2, \pi/2)$ phase (see Appendix F), which is why the low-lying sector of Fig. 8(b) has a different structure (and, in fact, higher GS energy per site; see Table II).

Turning to the quantum phase, the $N = 32$- and 64-site spectra give the onset of this phase around $J_\perp \simeq 0.23$ and $t \simeq 0.28$, respectively. Beyond this point, the spin-structure factor (not shown) is completely structureless, indicative of the absence of magnetic (classical) ordering. Since the imperfections in the present spin-ice model are expected to become irrelevant for large enough $J_\perp$, this phase must be the plaquette phase of the pure spin-ice model [11,71] and the pure Heisenberg model [85]. The standard diagnostics for this phase are the dimer-dimer (or energy-energy) correlations, and indeed, the correlation profiles of Fig. 9(c) show a strong $\mathbf{Q} = (\pi, \pi)$ response within one sublattice of empty plaquettes. This is consistent with the structure of the low-lying spectra that show two low-lying states with momenta $\mathbf{k} = 0$

and (π, π), which come almost on top of each other for $N = 64$ [see Fig. 8(c)]. Note that for $N = 32$, there is a third low-lying state (with $\mathbf{k} = 0$), which is, however, not related to the physics at the thermodynamic limit, but it is specific to the special topology of this cluster [86].

Further information about the two phases is given in Fig. 10, which shows the GS expectation values of the longitudinal and transverse NN spin-spin correlations for all symmetry-inequivalent bonds, as well as the square
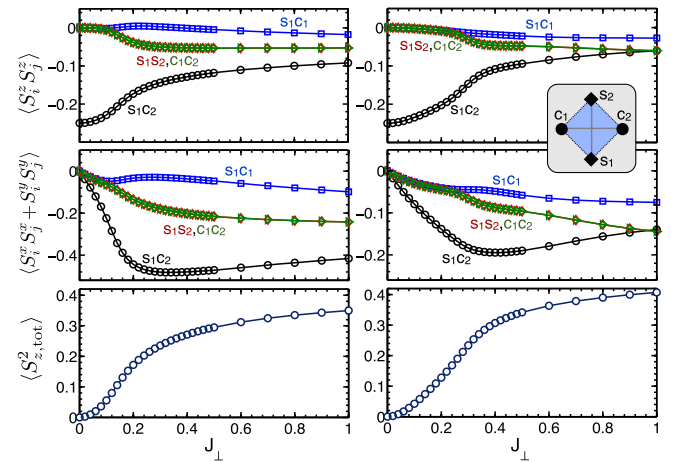

FIG. 10.   Various expectation values in the ground state of H for $N = 16$ (left column) and 32 (right column), for the cutoff $J_c = 0.001$. The first two panels in each column show the NN spin-spin correlations for all symmetry-inequivalent bonds (inset) in the longitudinal and transverse (xy) channel. The bottom panels show the square of the total magnetization per crossed plaquette, which is a measure of the weight from states outside the spin-ice manifold.

TABLE II. Results for the classical ground state at $t = 0$ from the classical minimization method of Sec. IV C 1, and exact diagonalizations. Here, N_{ints} is the total number of interaction terms (of the type $S_i^z S_j^z$) in the Hamiltonian, $\mathbf{Q}$ is the minimum of $\lambda_1(\mathbf{k})$ over the BZ, and $\mathbf{v}_1(\mathbf{Q})$ and $\lambda_1(\mathbf{Q})$ are the corresponding eigenvector [dashes indicate when the eigenvectors $\mathbf{v}_1(\mathbf{Q})$ cannot satisfy the spin-length constraint] and eigenvalue, respectively. The last line for each given N gives the corresponding ground-state energies per unit cell (multiplied by a factor of 4 to account for the unit spin length) as found by ED. Bold numbers indicate the cases with $N_{ints}(N) < N_{ints}(\infty)$ (for the given cutoff J_c) due to the finite size, showing that it is not safe to decrease the cutoff further.

N		Cutoff = 0.3	0.1	0.01	0.001
16	N_{ints}/N	3	**5**	**6.5**	**7.5**
	$\mathbf{Q}$	(π, π)	$(0, \pi), (\pi, 0)$	$\pm(-\pi/2, \pi/2)$	$\pm(-\pi/2, \pi/2)$
	$\mathbf{v}_1(\mathbf{Q})$	$(1, 1)/\sqrt{2}$	$(1,0), (0,1)$	$(1, \mp i)/\sqrt{2}$	$(1, \mp i)/\sqrt{2}$
	$\lambda_1(\mathbf{Q})$	-2.211504	-1.97784	-2.011411	-1.995727
	ED	-2.211504	-1.97784	-2.011411	-1.995727
32	N_{ints}/N	3	7	**10.5**	**15.5**
	$\mathbf{Q}$	(π, π)	$(0, \pi), (\pi, 0)$	$\pm(-\pi/2, \pi/2)$	$\pm(-\pi/2, \pi/2)$
	$\mathbf{v}_1(\mathbf{Q})$	$(1, 1)/\sqrt{2}$	$(1,0), (0,1)$	$(1, \mp i)/\sqrt{2}$	$(1, \mp i)/\sqrt{2}$
	$\lambda_1(\mathbf{Q})$	-2.211504	-2.271598	-2.089309	-2.056628
	ED	-2.211504	-2.271598	-2.089309	-2.056628
36	N_{ints}	3	7	**11.5**	**16.5**
	$\mathbf{Q}$	(π, π)	$\pm(-\pi, \pi/3)$	$\pm(\pi/3, -\pi/3)$	$\pm(\pi/3, -\pi/3)$
	$\mathbf{v}_1(\mathbf{Q})$	$(1, 1)/\sqrt{2}$	—	—	—
	$\lambda_1(\mathbf{Q})$	-2.211504	-2.03528	-1.95403	-1.94119
	ED	-2.211504	-1.8845151	-1.8803936	-1.8731703
64	N_{ints}/N	3	7	12	**25.5**
	$\mathbf{Q}$	(π, π)	$(0, \pi), (\pi, 0)$	$\pm(-\pi/2, \pi/2)$	$\pm(-\pi/2, \pi/2)$
	$\mathbf{v}_1(\mathbf{Q})$	$(1, 1)/\sqrt{2}$	$(1,0), (0,1)$	$(1, \mp i)/\sqrt{2}$	$(1, \mp i)/\sqrt{2}$
	$\lambda_1(\mathbf{Q})$	-2.211504	-2.271598	-2.166198	-2.108984
	ED	-2.211504	-2.271598	2.166198	-2.108984
72	N_{ints}/N	3	7	12	**27.5**
	$\mathbf{Q}$	(π, π)	$(0, \pi), (\pi, 0)$	$\pm(2\pi/3, -\pi/3)$	$\pm(2\pi/3, -\pi/3)$
	$\mathbf{v}_1(\mathbf{Q})$	$(1, 1)/\sqrt{2}$	$(1,0), (0,1)$	—	—
	$\lambda_1(\mathbf{Q})$	-2.211504	-2.271598	-2.075198	-2.03849
	ED	-2.211504	-2.271598	-2.04433866	-2.0137376
∞	N_{ints}/N	3	7	12	31
	$\mathbf{Q}$	(π, π)	$(0, \pi), (\pi, 0)$	$\pm0.473296(-\pi, \pi)$	$\pm0.4573374(-\pi, \pi)$
	$\mathbf{v}_1(\mathbf{Q})$	$(1, 1)/\sqrt{2}$	$(1,0), (0,1)$	—	—
	$\lambda_1(\mathbf{Q})$	-2.211504	-2.27159	-2.17273	-2.11938
	$\lambda_1(-\pi/2, \pi/2)$	-1.93452	-1.93452	-2.16620	-2.10609

magnetization of crossed plaquettes. The expectation values describe how the energy is distributed over the bonds and over the different directions in spin space, while the square magnetization is a measure of the admixture from states outside the spin-ice manifold. First, the NN correlations show that the spins fluctuate mostly along the z axis for small $J_\perp$, as expected. More importantly, most of the energy comes from antiferromagnetic bonds along one of the two diagonal directions (bonds labeled "$s_1 c_2$" in the inset of Fig. 10), which is a clear signature of the presence of strongly asymmetric spin-spin correlations in this regime. This asymmetry, which is inherited by the point-group symmetry (C_{2v}) of the model, is more directly revealed in the spin-structure factor discussed above. In addition, the qualitative change in the behavior of the NN correlations around $J_\perp \sim 0.2$ reflects the presence of the phase transition

in this region. Finally, the square of the total magnetization per crossed plaquette reveals that the spin-ice manifold remains well protected up to relatively high $J_\perp$.

C. Further insights in the classical limit $J_\perp = 0$

1. Momentum-space minimization

The nature of the classical phase and the role of the dipolar couplings can be understood in more detail by a closer examination of the limit $J_\perp = 0$ using a classical minimization treatment in momentum space [87–90]. The checkerboard lattice has a square Bravais lattice with two sites per unit cell. In the following, sites are labeled as $i \to (\mathbf{R}, \alpha)$, where $\mathbf{R}$ gives the position of the unit cell and $\alpha = 1$–2. For $J_\perp = 0$, we can replace $S_i^z \to \frac{1}{2}\sigma_i$, where $\sigma_i = \pm 1$. The total energy then reads $E = \frac{1}{4}E'$, where

$$E' = \frac{1}{2} \sum_{\mathbf{R}\,\mathbf{R'},\alpha\alpha'} J_{\mathbf{R}\alpha,\,\mathbf{R'}\alpha'} \sigma_{\mathbf{R},\alpha} \sigma_{\mathbf{R'},\alpha'}.$$

Using $\sigma_{\mathbf{R},\alpha} = \frac{1}{\sqrt{N_{uc}}} \sum_{\mathbf{k}} e^{i\,\mathbf{k}\cdot\mathbf{R}} \sigma_{\mathbf{k},\alpha}$ (where $N_{uc} = N/2$ is the number of unit cells) and $J_{\mathbf{R}\alpha,\,\mathbf{R'}\alpha'} = J_{\mathbf{R}-\mathbf{R'},\alpha\alpha'}$ (from translational invariance) yields

$$E' = \frac{1}{2} \sum_{\mathbf{k}} \sum_{\alpha\alpha'} \sigma_{\mathbf{k},\alpha} \Lambda_{\alpha\alpha'}(\mathbf{k}) \sigma_{-\mathbf{k},\alpha'},$$

where the 2×2 interaction matrix $\Lambda(\mathbf{k})$ is given by

$$\Lambda_{\alpha\alpha'}(\mathbf{k}) \equiv \sum_{\mathbf{r}} J_{\mathbf{r},\alpha\alpha'} e^{-i\,\mathbf{k}\cdot\mathbf{r}}.$$

Let us denote by $\lambda_{1,2}(\mathbf{k})$ and $\mathbf{v}_{1,2}(\mathbf{k})$ the eigenvalues and the corresponding (normalized) eigenvectors of $\Lambda(\mathbf{k})$, with $\lambda_1(\mathbf{k}) \leq \lambda_2(\mathbf{k})$. Minimizing $\lambda_1(\mathbf{k})$ over the entire Brillouin zone (BZ) of the model provides a lower bound for the energy [87–90]. The corresponding eigenvector is a faithful ground state, provided it satisfies the spin-length constraint at all sites.

The minimization can be done both for the infinite lattice and for the finite lattices studied by ED by simply scanning through the allowed momenta of each cluster. The latter are discussed in Appendix F and are useful for clarifying the various finite-size effects in our ED data. Here, we focus on the infinite-lattice case. Figure 11 shows the momentum dependence of the low-energy branch $\lambda_1(\mathbf{k})$ for cutoff values $J_c = 0.3, 0.1, 0.01$, and 0.001. For $J_c = 0.3$, which

amounts to keeping only the dominant NN couplings (i.e., three couplings per site), the minimum sits at $\mathbf{Q} = (\pi, \pi)$ and corresponds to the well-known Néel phase with antiferromagnetic (AFM) correlations along both the horizontal and the vertical directions of the lattice. This phase is stabilized by the imbalance in the NN imperfections, which favors the first two vertex configurations in Fig. 2(b). However, further-neighbor interactions destabilize the Néel phase and lead to a different minimum. For $J_c = 0.1$, which amounts to keeping seven interactions per site, the minimum of $\lambda_1(\mathbf{k})$ now sits at the two M points of the BZ, $\mathbf{Q} = (\pi, 0)$ and $(0, \pi)$, which correspond to a stripy AFM alignment of the spins in the horizontal or the vertical direction of the lattice.

Lowering J_c further shifts the minimum to two incommensurate (IC) positions, $\pm \mathbf{Q}_{IC}$, which are extremely close to the commensurate $\pm(-\pi/2, \pi/2)$ points. For example, for $J_c = 0.01$ (12 interactions per site), $J_c = 0.001$ (31 interactions per site), and $J_c = 10^{-6}$ (299 couplings per site), the minima sit, respectively, at $\mathbf{Q}_{IC} = 0.473(-\pi, \pi)$, $0.457(-\pi, \pi)$, and $0.462(-\pi, \pi)$. At the same time, the corresponding eigenvector $\mathbf{v}_1(\mathbf{Q}_{IC})$ cannot be used to construct a state satisfying the spin-length constraint at all sites of the system simultaneously. This means that the present method cannot deliver the true ground state of the system and that $\lambda_1(\mathbf{Q}_{IC})$ serves only as a lower energy bound.

Physically, the system may accommodate the tendency for incommensurate correlations by forming long-wavelength modulations of the local $(-\pi/2, \pi/2)$ order
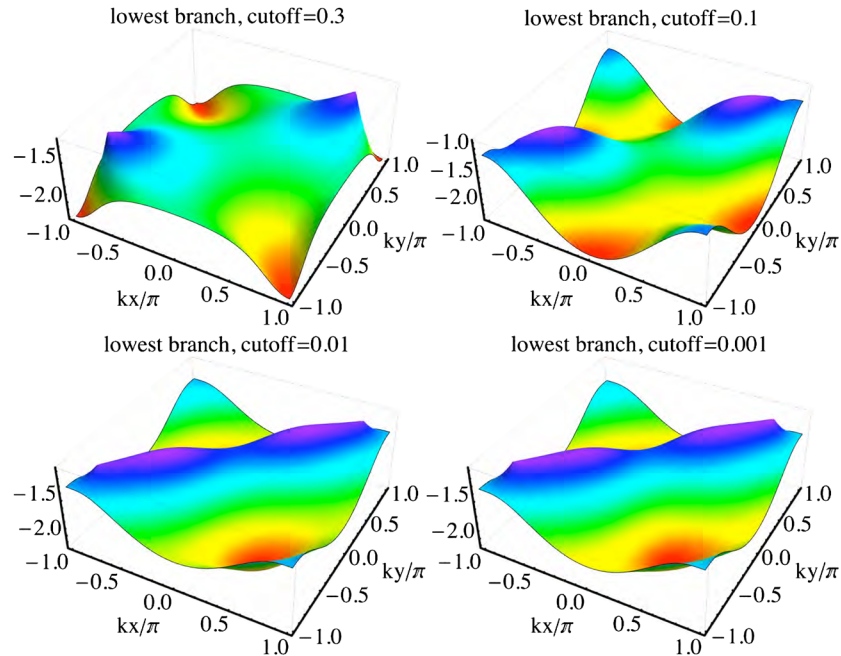

FIG. 11. Dispersion of the lowest eigenvalue $\lambda_1(\mathbf{k})$ (in units of $\tilde{V}_0$) of the dipolar interaction matrix $\Lambda(\mathbf{k})$ (in the thermodynamic limit) for four different cutoff values.

parameter, in analogy, e.g., to the anisotropic Ising model with competing interactions (the so-called ANNNI model) [91–94]. We should remark, however, that the energy landscape around the IC minimum is very flat, and its distance from $(-\pi/2, \pi/2)$ is very small; thus, in principle, such discommensurations (if any) should appear at much longer distances than the ones considered in our finite-lattice calculations and, indeed, at length scales over which cold-atom realizations are not uniform (in both density and interaction patterns) on account of the parabolic confining potential. To confirm this point, we have performed classical Monte Carlo (CMC) simulations on $N = 2 \times L \times L$-site clusters with periodic boundary conditions (see details in Appendix G). All results up to $L = 36$ consistently give the $(-\pi/2, \pi/2)$ state without any sign of domain-wall discommensurations, implying that, at least for these distances, the system locks in to the closest commensurate $\mathbf{Q} = (-\pi/2, \pi/2)$ phase.

2. Thermal phase transition into a classical Coulomb phase

Given the finite energy gap above the commensurate $\mathbf{Q} = (-\pi/2, \pi/2)$ state at $J_\perp = 0$ (see Fig. 8), one expects that this phase survives against thermal fluctuations up to a finite temperature T_C. To confirm this picture, and to find the numerical value of T_C, we have performed classical MC simulations at finite temperatures. The first two panels of Fig. 12 show the T dependence of the structure factor $\mathcal{S}(\mathbf{Q})$ at $\mathbf{Q} = (-\pi/2, \pi/2)$ and the specific heat per site for systems up to $N = 2 \times 28 \times 28$ sites. The results demonstrate clearly the thermal phase transition, with $T_C \simeq 0.185$. The third panel shows the T dependence of the three different types of crossed plaquette configurations: the ice-rule 2 in - 2 out states and the defective 3 in - 1 out

(or 3 out - 1 in) states and 4-in (or 4-out). The defects are almost entirely of the 3 up - 1 down type, but their density remains very small up to the transition temperature (about 5%). So, the classical phase gives way to a Coulomb gas [65,66], an approximate realization of a classical Coulomb phase, with only a very small density of defects. This phase is marginally confined on account of the logarithmic nature of the interactions between the defects; given the non-vanishing defect density above T_C, their correlations are expected to exhibit a screened (Debye) form [95].

V. QUANTUM DIMER MODELS WITH RYDBERG ATOMS: BEYOND QUANTUM ICE

A. Simple interactions, complicated lattices

As we have shown in the spin-ice example, weakly Rydberg-dressed atoms in optical lattices provide a perfect platform to investigate quantum magnetism in AMO settings. The procedure can be extended to a series of 2D and 3D models using isotropic interactions, either with s states (whose corresponding frozen regimes have already been accessed in a series of experiments [23–37,96]) or p states (with out-of-plane polarization in the 2D case) combined with complicated lattice structures. This way, the complication of realizing a fine-tuned interaction pattern is transferred to a complicated lattice geometry, which might be realized if the corresponding light pattern is realizable.

The fundamental features of those complicated lattices include the fact that isotropic interactions with a sharp plateau are sufficient to define a classical limit where there is a set of degenerate classical ground states, increasing extensively with system size. Given the shape of the interactions, one can identify the possible lattices as follows. First, we define b as the largest distance between
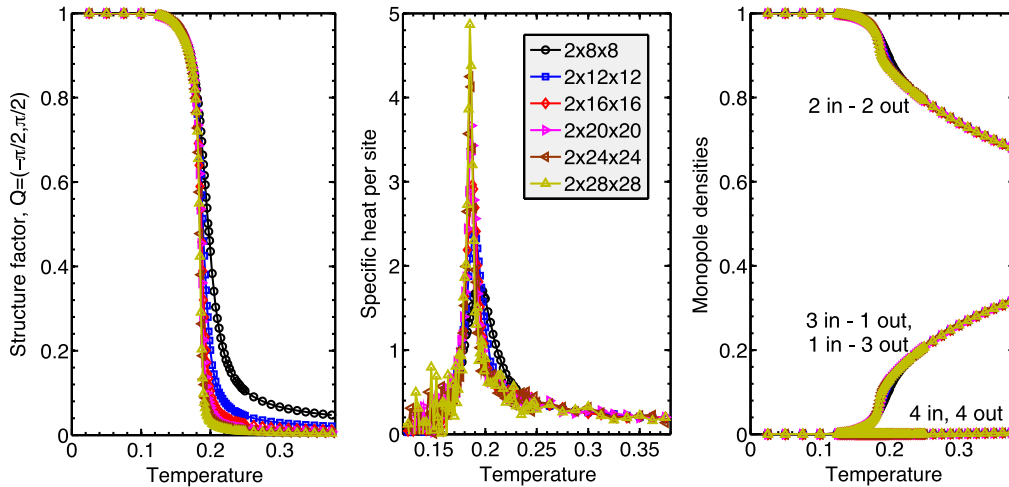

FIG. 12.   Temperature dependence of the structure factor $\mathcal{S}(\mathbf{Q})$ (left panel); the specific heat per site, in units of Boltzmann's constant k_B (middle panel), and the monopole densities for systems up to $N = 2 \times 28 \times 28$ sites (right panel), for $J_\perp = 0$ and the cutoff $J_c = 0.001$. Temperature is given in units of $\tilde{V}_0$.
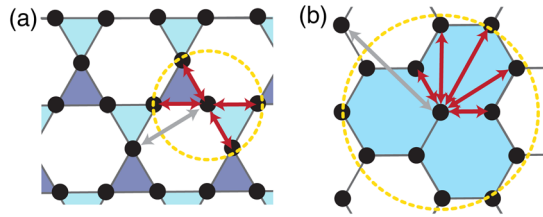
FIG. 13.   Lattices possessing the properties discussed in Sec. V A: Panel (a) shows a Kagome lattice with triangles as gauge cells (shaded area), and panel (b) shows a honeycomb lattice with hexagons as gauge cells. In both cases, the maximal intraplaquette Euclidean distance (yellow dashed circle) is smaller than the minimal interplaquette distance (gray arrow). The radius of the needed plateaulike interaction is described by the yellow circles.

sites belonging to the same simplices [8] (or gauge cell), that is, the unit cell where the Gauss law of interest is defined (in the spin-ice case, these are the squares with crosses). Second, we define c as the smallest distance between sites that do not belong to the same gauge cell. It is then clear that, in the case where $b < c$, a plateau interaction in the range $b < r_{bc} < c$ can generate the desired constraint in each gauge cell. In the case that this is not true (like, e.g., in the square-ice case), additional features are needed, such as angular dependence.

Some examples of the lattices that satisfy the previous property are illustrated in Fig. 13, together with the corresponding gauge cells. The list includes several 2D lattices that have already been realized in AMO settings, such as the Kagome lattice with triangular gauge cells (but not with hexagonal gauge cells), the ruby lattice, and the honeycomb

lattice. In the 3D case, a simple example is the pyrochlore lattice, already discussed in Ref. [39] in the context of polar gases. Interestingly, in this former case, dipolar interactions behave in a very similar manner to simple plateaulike ones because of their symmetry content [97].

Once taken at a filling factor of an integer number of particles per gauge cell for the underlying Bose-Hubbard Hamiltonian, all of those lattices generate quantum dimer or quantum loop models [8] in perturbation theory. These are naturally described by emergent gauge theories: However, the gauge symmetry itself is not always straightforwardly determined, given the gauge symmetry of the microscopic constituents [98]. The procedure to derive the proper dimer-model dynamics, given a lattice and an Ising constraint, is outlined in Ref. [8]. Below, we illustrate a simple example of how complicated lattices can meet simple interactions to let a quantum dimer model emerge by focusing on the concrete example of the 4–8 lattice.

B. Emergent quantum dimer dynamics on a 4–8 lattice from an *XXZ* model

The 4–8 lattice (also known as the CAVO lattice) [99] represents a useful example to illustrate how the combination of a complicated lattice with simple Ising interactions can lead to intriguing quantum dynamics. The lattice structure for the underlying bosons from which we start is the squagome lattice [100,101], illustrated in Fig. 14: Once the triangles are identified as the gauge cells, it is easy to see that $b = a$, $c = \sqrt{2}a$, so a plateau interaction in the range $1 < r/a < \sqrt{2}$ can indeed enforce constraints on the gauge cells. Since each site is shared by
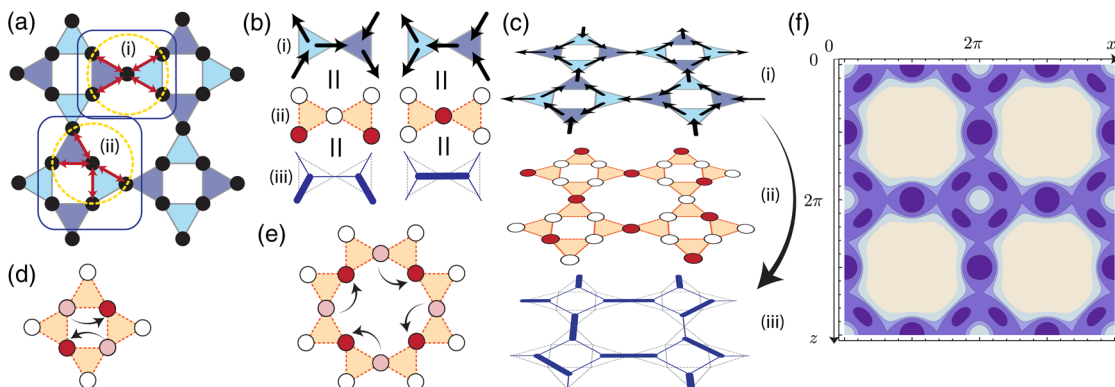

FIG. 14.   Configuration space of the squagome lattice and gauge-invariant dynamics: (a) Atoms are trapped into a squagome pattern (filled-black circles) and interact with NN atoms (red arrows), which are all the same distance apart (yellow dashed circle). Triangular gauge cells are indicated as shaded areas, in an alternating pattern of light blue and violet. Panel (b) describes possible gauge-invariant configurations [from Eq. (18)], including one with two flux vectors pointing outwards (inwards) on a light-blue (violet) gauge-cell map onto a configuration where a single site on each triangle is occupied (red circle) and two lattice sites are unoccupied (white circles). Here, an arrow pointing from a violet triangle to a light-blue triangle corresponds to an occupied lattice site and, vice versa, to an empty lattice site. This can be further mapped to a quantum dimer model on the 4–8 lattice. The new sites are defined at the center of each triangle: The bond variable between them is either empty (thin blue line) or a dimer (thick blue line), depending on the original occupation of the site shared by the triangles. Panel (c) illustrates a full gauge-invariant configuration. Quantum fluctuations induce nontrivial dynamics around both the square (d) and octagonal (e) plaquettes, described by Eqs. (20) and (21). Panel (f) shows the optical lattice pattern of Eq. (22), as described in the text. Darker areas correspond to deeper potentials.

three gauge cells, a filling fraction of $n = 1/3$ atoms per site, combined with the plateau interactions, will generate a degenerate manifold $\mathcal{H}_{4\text{--}8}$ of classical ground states, where for each triangle, a single site is occupied [see Fig. 14(b)].

When formulated in spin language with $S_j^z = n_j - 1/2$, the Hamiltonian

$$H_{4\text{--}8}^{Is} = J_z \sum_\Delta \sum_{\{i,j\}\in\Delta} S_j^z S_i^z \qquad (17)$$

has (trivially) a set of $U(1)$-like conserved charges at each triangle, that is,

$$G_\Delta = \sum_{j\in\Delta} S_j^z + 1/2, \qquad G_\Delta|\psi\rangle = 0, \quad \forall \; |\psi\rangle \in \mathcal{H}_{4\text{--}8}. \qquad (18)$$

Once an additional small term inducing quantum fluctuations is introduced,

$$H_{4\text{--}8}^{Ex} = J \sum_\Box \sum_{\{i,j\}\in\Box} S_j^+ S_i^- + \tilde{J} \sum_\bigcirc \sum_{\{i,j\}\in\bigcirc} S_j^+ S_i^- \qquad (19)$$

tunneling between the different classical degenerate minima becomes possible within perturbation theory, while still preserving the set of conserved charges in Eq. (18). Notice that we used two different matrix elements for particle tunneling around the squares (J) and around the octagons ($\tilde{J}$). Two kinds of moves are allowed. At second order, two particles sitting along a diagonal of a square plaquette can resonantly flip to sit on the other diagonal:

$$H^\Box \simeq -\frac{J^2}{J_z}(S_1^+ S_2^- S_3^+ S_4^- + \text{H.c.}), \qquad (20)$$

where we have numbered the sites of the square plaquette in clockwise order. The next nonvanishing contribution takes place at fourth order, where particles sitting at the edges of each octagonal plaquette can be rearranged via an extended ring exchange:

$$H^\bigcirc \simeq -3\frac{\tilde{J}^4}{J_z^3}(S_1^+ S_2^- S_3^+ S_4^- S_5^+ S_6^- S_7^+ S_8^- + \text{h.c.}). \qquad (21)$$

where we have numbered the sites of the octagonal plaquette in clockwise order. The two terms are illustrated in Figs. 14(d) and 14(e). We now reformulate the problem in terms of dimer models, which allows us to set up a proper description in terms of effective degrees of freedom. In order to do that, we follow the procedure exemplified in Refs. [8,102–104] and illustrated in Figs. 14(b) and 14(c): We define a new lattice, the so-called simplex lattice, whose vertices are the middle points of each gauge cell and whose bonds connect vertices of gauge cells that share a single

site—each bond sits on a vertex of the original lattice. Then, we introduce dimer variables on the bonds as follows: (i) If a bond sits on a site that is occupied by a boson, we draw a dimer; (ii) if not, we leave the bond empty. Thus, the Gauss law of Eq. (18) is easily reformulated as a conservation law of a single dimer at each vertex.

The lattice on top of which the quantum dimer model is defined is then a 4–8 lattice: As it is bipartite, the corresponding low-energy theory is a $U(1)$ gauge theory, which can then display different confined phases as a function of the two kinetic energy terms for the dimers $H^\bigcirc$ and $H^\Box$. This setup might then constitute a perfect setting for the investigation of the competition between different RVB solid orders and the transitions between them. The corresponding periodic structure can either be realized using digital-micromirror-devices (DMD) [67] or by using an optical potential of the form

$$V(x,z) = 4V_1(x+z, x-z) + V_2(x,z), \qquad (22)$$

where

$$V_1(x,z) = \cos(\pi x)^2 + \cos(\pi z)^2 \\ - 2\cos(0.55)\cos(\pi x)\cos(\pi z) \qquad (23)$$

is a 2D lattice created by two 1D standing waves with a phase difference $\phi = 0.55$ and antiparallel polarizations $\mathbf{e}_1 \cdot \mathbf{e}_2 = -1$. The second 2D lattice is created by lasers with 3 times the frequency and orthogonal polarization,

$$V_2(x,z) = \cos(3\pi x)^2 + \cos(3\pi z)^2. \qquad (24)$$

Both lattices are rotated by 45 degrees, respectively. The full lattice structure is illustrated in Fig. 14(f), and it realizes the squagome lattice potential of interest.

VI. CONCLUSIONS AND OUTLOOK

In summary, we have shown how dynamical gauge fields emerging from frustration can be ideally realized in cold-atom systems by employing optical lattices combined with Rydberg interactions. This allows us to probe gauge-theory phenomena in a variety of models. In particular, we analyzed in detail the case of quantum square ice, a paradigmatic example of frustrated statistical mechanics, both at the few-body level and at the many-body level.

From the atomic-physics side, the key element of our implementation is the tunable interaction pattern generated by Rydberg p states and local polarizations due to tensor polarizabilities. Prominent atomic-physics features can be exploited in order to generate (repulsive) anisotropic interactions that allow us to enforce the complex gauge constraints of square-ice models. The possibility of generating such anisotropic interaction patterns enriches the cold-atom Hubbard toolbox of yet another potential feature,

which can find different applications in many-body physics even beyond engineering complicated and fine-tuned lattice constraints. It paves the way for the realization of different constrained dynamics, in particular, quantum dimer models on complicated lattices.

From the many-body side, we have provided numerical evidence that typical imperfections generated by the Rydberg interactions still allow the observation of a non-trivial state of matter, a plaquette valence bond crystal. Moreover, we have shown how a cold-atom-suited detection technique can be identified, by performing parity measurements along the plaquettes, which directly identifies the spontaneous symmetry breaking of a discrete lattice symmetry. Even in the absence of quantum dynamics, the engineered interactions stabilize a magnetically ordered state with a large unit cell at low temperatures, which gives way to a classical Coulomb gas, a marginally confining two-dimensional Coulomb phase with a small but nonzero density of charges in the form of thermally activated plaquettes violating the ice rule.

Different directions can be pursued further, following the lines discussed here. A first, interesting extension would be to understand whether different kinds of anisotropic interactions can play a significant role in engineered Ising constraints in cold-atom systems. In particular, anisotropic interactions between Rydberg d states of ^{87}Rb atoms have recently been demonstrated in Ref. [37]: As their angular dependence differs from the one discussed here, it can constitute yet another tool in order to realize complicated, fine-tuned interaction patterns. Additionally, the present proposal, which generates pure gauge theories, can be combined in a modular way with previous ones [105] in such a way that either fermionic or bosonic matter can be included in the dynamics. This would extend the toolkit of quantum simulation of lattice gauge theories within the quantum-link model formalism. On the one hand, quantum simulation of QED$_3$ models with different flavor degrees of freedom could be foreseen [106]. On the other hand, the combination of bosonic fields (as, e.g., in Ref. [105]) with the current proposal would allow for the exploration of the Fradkin-Shenker scenario of Higgs physics in 2D [107] and possibly in more exotic geometries. Finally, cold-atom realizations can also provide a suitable platform for the investigation of *dynamical* effects in quantum dimer models and gauge theories in general; it would be interesting to see whether simple observables and experimental procedures can be implemented to describe complex many-body phenomena such as string dynamics [108] in the presence of static charges [40], or the dynamical properties of thermally activated monopoles on top of a vacuum state.

ACKNOWLEDGMENTS

APPENDIX A: EFFECT OF THE AC-STARK LASERS ON THE GROUND STATE

The AC-Stark lasers introduced in Sec. III A create an additional trapping potential, $V_{AC}(\mathbf{r}_i)|g\rangle\langle g|_i$, for ground-state atoms with minima that are not commensurate with the initial trapping lattice. In order not to distort the desired lattice structure, this additional potential must not be larger than the initial trapping potential. The dominant effect comes from a second-order Stark effect by off-resonantly coupling the $5S$ state to the first excited state $5P$, and it is given by $V_{AC} = \Omega_{5s5p}^2/(2\Delta_{5s5p})$, with Rabi frequency $\Omega_{5s5p} = 2d_{5s5p}\mathcal{E}/\hbar$ and detuning $\Delta_{5s5p} = 2\pi c(\lambda_{5s5p}^{-1} - \lambda_{AC}^{-1})$. Here, $d_{5s5p} = \langle 5S|d|5P\rangle$ is the transition dipole matrix element and λ_{5s5p} the transition wavelength. Figure 15(a) shows the desired trapping lattice created by two counterpropagating laser beams which form a ground-state potential $V_{trap}(z,x) = \cos^2 kz + \cos^2 kx$. The dashed black lines indicate the 0.9-level lines of the AC-Stark potential $V_{AC}(z,x) = \cos^2[k_{AC}(x-y)/\sqrt{2}] + \sin^2[k_{AC}(x+y)/\sqrt{2}]$, with $k_{AC} = k/\sqrt{2}$. The maxima are localized at the ● and ■ lattice sites, respectively, as required in Sec. III A. Figure 15(b) shows the total potential, $V_{tot} = V_{trap} + \alpha V_{AC}$, in the case of equal strength, i.e., $\alpha = 1$. The insets on top show the 1D
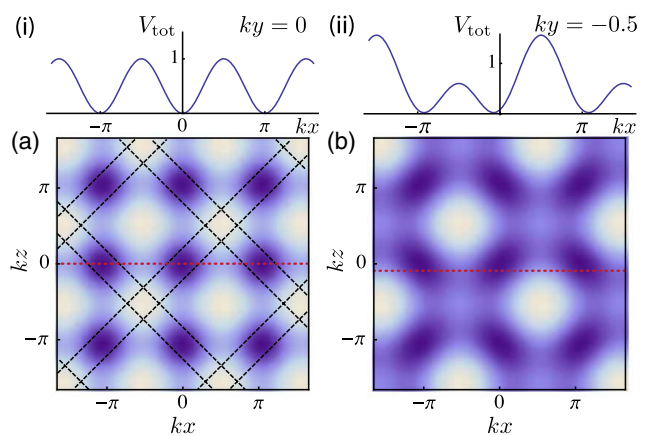

FIG. 15. Contour plots of the total trapping potential $V_{tot}(x,z)$, (a) without the AC-Stark potential ($\alpha = 0$) and (b) with the AC-Stark potential ($\alpha = 1$). The black dashed lines in (a) show the 0.9-level lines of the AC-Stark potential V_{AC}. The insets (i) and (ii) show the 1D potential along the red dotted lines for (i) $ky = 0$ and (ii) $ky = -0.5$.

potential along the (i) $ky = 0$ and (ii) $ky = -0.5$ lines [red dotted lines in Figs. 15(a) and 15(b)]. In the case of equal strength of the trapping lattice and the additional lattice created by the AC-Stark lasers, the potential minima are still located at the same position, but slightly elongated. Note that the potential barrier between neighboring lattice sites is about half as small as without the additional AC-Stark laser. This will lead to higher tunneling rates compared to the case without the AC-Stark laser.

APPENDIX B: GLOBAL RYDBERG LASER EXCITATION

In the following, we show that it is possible to weakly admix the locally polarized Rydberg states of Sec. III A to the electronic ground state $|g\rangle$ using a *single* laser with a wave vector $\mathbf{k} \sim \mathbf{y}$ and polarization σ_+ (see Fig. 4),

$$H_L = \frac{\Omega_R}{2}[|g\rangle_{yy}\langle nP_{3/2}, 3/2| + \text{H.c.}]. \quad (B1)$$

In the local x and z bases, this laser will couple to all four m_j levels with different weights, i.e.,

$$\left|\frac{3}{2}\right\rangle_y = \frac{1}{2\sqrt{2}}\left[\left|\frac{3}{2}\right\rangle_z + i\sqrt{3}\left|\frac{1}{2}\right\rangle_z - \sqrt{3}\left|-\frac{1}{2}\right\rangle_z - i\left|-\frac{3}{2}\right\rangle_z\right], \quad (B2)$$

$$\left|\frac{3}{2}\right\rangle_y = \frac{1}{2\sqrt{2}}\left[e^{-3i\pi/4}\left|\frac{3}{2}\right\rangle_x + \sqrt{3}e^{-i\pi/4}\left|\frac{1}{2}\right\rangle_x\right.$$
$$\left. + \sqrt{3}e^{i\pi/4}\left|-\frac{1}{2}\right\rangle_x + e^{3i\pi/4}\left|-\frac{3}{2}\right\rangle_x\right], \quad (B3)$$

where we used the irreducible representation of a rotation in the $j = 3/2$ subspace, $D[\mathcal{R}(\alpha, \beta, \gamma)] = e^{-i\alpha J_z}e^{-i\beta J_y}e^{-i\gamma J_z}$.

Since the states $|m \neq 3/2\rangle_{z,x}$ are energetically separated by at least E_{AC} from the $|m = 3/2\rangle$ state, a laser with detuning $\Delta_R \ll E_{\text{AC}}$ and wave vector $\mathbf{k} \sim \mathbf{y}$ will selectively admix the states $|3/2\rangle_z$ and $|3/2\rangle_x$ at lattice sites ● and ■, respectively, to the ground state $|g\rangle$ with an effective Rabi frequency $\Omega_R/(2\sqrt{2})$.

APPENDIX C: VAN DER WAALS INTERACTIONS

In this appendix, we briefly summarize the technical details in order to calculate the angular-dependent van der Waals interactions of Sec. III B. Because of the odd parity of the electric dipole operators $d_\mu^{(i)}$ and $d_\nu^{(j)}$, the dipole-dipole interaction V_{dd} of Eq. (11) can only couple states with initial angular (total) momentum ℓ (j) to states with new angular (total) momentum $\ell \pm 1$ (j or $j \pm 1$).

Therefore, the number of possible "channels" $n\ell j m_1 + n\ell j m_2 \longrightarrow n'\ell' j' m' + n''\ell'' j'' m''$ for which the matrix element $\langle n\ell j m_1; n\ell j m_2|V_{\text{dd}}^{(ij)}|n'\ell' j' m'; n''\ell'' j'' m''\rangle$ is nonzero are limited. While there is no selection rule for possible final principal quantum numbers n' and n'' which solely determine the overall strength of the matrix element, the dipole-dipole matrix element is only nonzero if the magnetic quantum numbers and the spherical component of the dipole operator fulfill $m_1 + \mu = m'$ and $m_2 + \nu = m''$. If the energy difference $\delta_{\alpha\beta} = E(\alpha) + E(\beta) - 2E(n\ell j)$ between the initial states $n\ell j$ and the intermediate states $\alpha \equiv n_\alpha \ell_\alpha j_\alpha m_\alpha$ and $\beta \equiv n_\beta \ell_\beta j_\beta m_\beta$ of the atoms is larger than the dipole-dipole matrix element connecting those states, the dominant interaction is of van der Waals type, which arises from V_{dd} in second-order perturbation,

$$\hat{V}_{\text{vdW}} = \hat{P}_{12}\sum_{\alpha\beta}\frac{\hat{V}_{\text{dd}}\hat{Q}_{\alpha,\beta}\hat{V}_{\text{dd}}}{\delta_{\alpha\beta}}\hat{P}_{34}. \quad (C1)$$

Here, $\hat{V}_{\text{vdW}}$ is an operator acting in the degenerate manifold of magnetic sublevels, with $\hat{P}_{ij} = |n\ell j m_i, n\ell j m_j\rangle\langle n\ell j m_i, n\ell j m_j|$ a projector into the $n\ell j$ manifold and $\hat{Q}_{\alpha,\beta} = |\alpha, \beta\rangle\langle\alpha, \beta|$ a projector on a specific state in the complementary space. The sum is over all two-atom energy levels, where the indices $\alpha \equiv n_\alpha \ell_\alpha j_\alpha m_\alpha$ and $\beta \equiv n_\beta \ell_\beta j_\beta m_\beta$ denote a full set of quantum numbers that specify the states. Because of the electric dipole selection rules discussed above, this sum can be split up into channels denoted by $\nu = (\ell_\alpha, j_\alpha; \ell_\beta, j_\beta)$. Equation (C1) can be written as $\hat{V}_{\text{vdW}} = \sum_\nu C_6^{(\nu)}\mathcal{D}_\nu(\vartheta, \varphi)/r^6$, where $C_6^{(\nu)}$ contains the radial part of the matrix elements,

$$C_6^{(\nu)} = \sum_{n_\alpha, n_\beta}\frac{\mathcal{R}_1^\alpha \mathcal{R}_2^\beta \mathcal{R}_3^\alpha \mathcal{R}_4^\beta}{\delta_{\alpha\beta}}, \quad (C2)$$

which accounts for the overall strength of the interaction and is independent of the magnetic quantum numbers. Here, $\mathcal{R}_i^j = \int dr r^2 \psi_{n_i, \ell_i, j_i}(r)^* r \psi_{n_j, \ell_j, j_j}(r)$ is the radial integral calculated with radial wave functions $\psi_{n_j, \ell_j, j_j}(r)$ obtained using the model potential from Ref. [109]. The matrix

$$\mathcal{D}_\nu(\vartheta, \varphi) = \hat{P}_{12}\sum_{m_\alpha, m_\beta}\mathcal{M}_\nu \hat{Q}_{\alpha,\beta}\mathcal{M}_\nu \hat{P}_{34}, \quad (C3)$$

on the other hand, is a matrix in the subspace of magnetic quantum numbers, which contains the relative angles between the two atoms ($s = 1/2$),

$$\langle m_1, m_2 | \mathcal{M}_\nu | m_\alpha, m_\beta \rangle = (-)^{s-m_1} \sqrt{\prod_{i=1,\alpha} (2\ell_i + 1)(2j_i + 1)} \begin{Bmatrix} \ell_1 & \ell_\alpha & 1 \\ j_\alpha & j_1 & s \end{Bmatrix} \begin{pmatrix} \ell_\alpha & 1 & \ell_1 \\ 0 & 0 & 0 \end{pmatrix}$$

$$\times (-)^{s-m_2} \sqrt{\prod_{i=2,\beta} (2\ell_i + 1)(2j_i + 1)} \begin{Bmatrix} \ell_2 & \ell_\beta & 1 \\ j_\beta & j_2 & s \end{Bmatrix} \begin{pmatrix} \ell_\beta & 1 & \ell_2 \\ 0 & 0 & 0 \end{pmatrix}$$

$$\times \left(-\sqrt{\frac{24\pi}{5}} \sum_{\mu,\nu} C^{1,1;2}_{\mu,\nu;\mu+\nu} \begin{pmatrix} j_\alpha & 1 & j_1 \\ m_\alpha & \mu & -m_1 \end{pmatrix} \begin{pmatrix} j_\beta & 1 & j_2 \\ m_\beta & \nu & m_2 \end{pmatrix} Y_2^{\mu+\nu}(\vartheta, \varphi)^* \right). \tag{C4}$$

As an example, we show the $\mathcal{D}_1$ matrix for the first channel $P_{3/2} + P_{3/2} \longrightarrow S_{1/2} + S_{1/2}$,

$$\mathcal{D}_1 = \begin{pmatrix} \frac{1}{4} \sin^4 \vartheta & -\frac{1}{2\sqrt{3}} \cos \vartheta \sin^3 \vartheta & \frac{\sin^2 \vartheta}{24\sqrt{3}} (3 \cos 2\vartheta + 1) & 0 \\ -\frac{1}{2\sqrt{3}} \cos \vartheta \sin^3 \vartheta & \frac{1}{12} (\sin^4 \vartheta + \sin^2 2\vartheta) & -\frac{1}{9} \cos \vartheta \sin \vartheta & \frac{\sin^2 \vartheta}{24\sqrt{3}} (3 \cos 2\vartheta + 1) \\ \frac{\sin^2 \vartheta}{24\sqrt{3}} (3 \cos 2\vartheta + 1) & -\frac{1}{9} \cos \vartheta \sin \vartheta & \frac{1}{864} (12 \cos 2\vartheta - 27 \cos 4\vartheta + 47) & -\frac{\sin 2\vartheta}{24\sqrt{3}} (3 \cos 2\vartheta + 1) \\ 0 & \frac{\sin^2 \vartheta}{24\sqrt{3}} (3 \cos 2\vartheta + 1) & -\frac{\sin 2\vartheta}{24\sqrt{3}} (3 \cos 2\vartheta + 1) & \frac{1}{144} (3 \cos 2\vartheta + 1)^2 \end{pmatrix} \tag{C5}$$

in the subspace of states $|\frac{3}{2}, \frac{3}{2}\rangle$, $|\frac{3}{2}, \frac{1}{2}\rangle$, $|\frac{3}{2}, -\frac{1}{2}\rangle$, and $|\frac{3}{2}, -\frac{3}{2}\rangle$, where the first atom is fixed in the $m = 3/2$ state. In general, one has to diagonalize the operator $\hat{V}_{\text{vdW}}$ in the degenerate Zeeman subspace in order to obtain the new eigenenergies and eigenstates in the presence of interactions. If an external electric or magnetic field separates an initial two-atom state $|m_1, m_2\rangle$ from all other Zeeman sublevels such that the energy difference is larger than the vdW coupling matrix elements, then it is possible to simply take expectation values of $V^{(n)}_{m_1, m_2}(\mathbf{r}) = \langle m_1, m_2 | \hat{V}_{\text{vdW}} | m_1, m_2 \rangle$ in order to obtain the interaction potential of two atoms initially in the $|m_1, m_2\rangle$ state.

APPENDIX D: MIXED INTERACTIONS

In the following, we show how to calculate the mixed interactions $V_{\bullet\blacksquare}(r, \vartheta)$ introduced in Sec. III B between the *locally* polarized Rydberg states $|\bullet\rangle \equiv |nP_{3/2}, 3/2\rangle_{\mathbf{z}}$ and $|\blacksquare\rangle \equiv |nP_{3/2}, 3/2\rangle_{\mathbf{x}}$. Here, the indices z and x denote the local quantization axis of the state. We work in the z basis. Rotating the latter state into the z basis using the irreducible representation $D^{(3/2)}[\mathcal{R}(\hat{\mathbf{y}}, \pi/2)]^{-1}$ of a rotation around $\mathbf{y}$ by an angle of $\pi/2$ in the $j = \frac{3}{2}$ space yields

$$|\blacksquare\rangle = \frac{1}{2\sqrt{2}} \left[\left| \frac{3}{2} \right\rangle_{\mathbf{z}} - \sqrt{3} \left| \frac{1}{2} \right\rangle_{\mathbf{z}} + \sqrt{3} \left| -\frac{1}{2} \right\rangle_{\mathbf{z}} - \left| -\frac{3}{2} \right\rangle_{\mathbf{z}} \right], \tag{D1}$$

where $|m\rangle_{\mathbf{z}} \equiv |nP_{3/2}, m\rangle_{\mathbf{z}}$. The state $|\blacksquare\rangle = |nP_{3/2}, 3/2\rangle_{\mathbf{x}} = \sum_m c_m |nP_{3/2}, m\rangle_{\mathbf{z}}$ is thus a superposition of different m_j states in the z basis. Interactions between two atoms in a $|\blacksquare\bullet\rangle$ or $|\blacksquare\blacksquare\rangle$ state can be calculated by evaluating the corresponding matrix elements of Eq. (C1), which requires us to compute van der Waals interactions between atoms in different m_j states, e.g.,

$$\langle \bullet\blacksquare | V_{\text{vdW}} | \bullet\blacksquare \rangle = \sum_{m,m'} c_{m'} c_m^* \left\langle \frac{3}{2}, m | V_{\text{vdW}} | \frac{3}{2}, m' \right\rangle. \tag{D2}$$

The angular dependence of the van der Waals interaction between two Rydberg atoms in a $|\bullet\bullet\rangle$ or in a $|\blacksquare\blacksquare\rangle$ state, $V_{\bullet\bullet}(r, \vartheta) = V_{\blacksquare\blacksquare}(r, \vartheta - \pi/2) \sim \sin^4 \vartheta / r^6$, is the same up to a rotation by 90 degrees and shows the typical anisotropic behavior discussed in Sec. III B [see solid lines in Fig. 5(a)]. On the other hand, the angular dependence of the mixed interactions between two Rydberg atoms in a $|\blacksquare\bullet\rangle$ state, shown in Fig. 16(a), exhibits two asymmetric maxima at $\vartheta = \pm\pi/4$. The asymmetry arises from off-diagonal matrix elements, e.g., $\langle \frac{3}{2}, \frac{1}{2} | \hat{V}_{\text{vdW}} | \frac{3}{2}, -\frac{1}{2} \rangle \sim \sin 2\vartheta$. Note that the actual strength of the interaction only affects the Condon radius r_c [see Eq. (15) and not the energy shift $\tilde{V}_0$ [see Eq. (14) and discussion thereof] for $r \to 0$. Panel (c) of Fig. 16 shows a contour plot of the mixed interaction, $\tilde{V}_{\bullet\blacksquare}/\tilde{V}_0$ of Eq. (14), between the dressed ground-state atoms $|\bullet\rangle$ in the middle and the surrounding $|\blacksquare\rangle$ atoms. Interactions with the neighboring $|\blacksquare\rangle$ atoms (red solid arrows) are strong, $\sim\tilde{V}_0$, while interactions with next-nearest-neighbor $|\blacksquare\rangle$ atoms (red dotted arrows) are strongly suppressed because of the plateau structure of the potential.
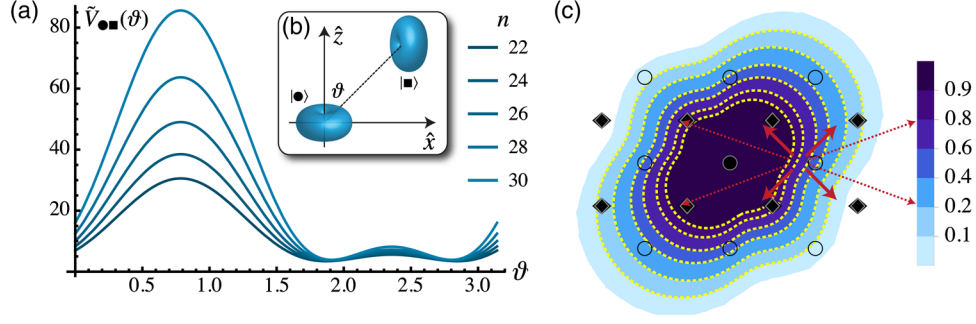
FIG. 16. (a) Angular part $A_{\bullet\blacksquare}^{(n)}(\vartheta)$ of the van der Waals interaction, $V_{\bullet\blacksquare}^{(n)}(r,\vartheta) = (n - \delta_{n\ell j})^{11} A_{\bullet\blacksquare}^{(n)}(\vartheta)/r^6$, between a pair of ^{87}Rb atoms in the $|r_\bullet\rangle = |nP_{3/2}, 3/2\rangle_z$ and $|r_\blacksquare\rangle = |nP_{3/2}, 3/2\rangle_x$ Rydberg states of ^{87}Rb (solid lines). We plot the rescaled interaction energy $A_{\bullet\blacksquare}^{(n)}(\vartheta)$ as a function of the angle ϑ for various values of the principal quantum number n, with δ the quantum defect. (b) Cartoon of the states and definition of the angle ϑ. (c) Contour plot of the effective interaction $\tilde{V}_{\bullet\blacksquare}^{(n)}(r,\vartheta)/\tilde{V}_0$ between the dressed ground-state atom $|\bullet\rangle$ in the middle and the NN $|\blacksquare\rangle$ atoms (red arrows) and the NNN $|\blacksquare\rangle$ atoms (red dotted arrows).

APPENDIX E: FINITE-SIZE CLUSTERS

In our exact diagonalizations, we have considered the following checkerboard clusters with periodic boundary conditions:

N	$\mathbf{T}_1$	$\mathbf{T}_2$	$\mathbf{G}_1$	$\mathbf{G}_2$	$\mathcal{D}_{\text{full}}^{S_z=0}$	$\mathcal{D}_{\text{spin-ice}}$
16	(2,2)	(−2,2)	$(\pi/2,\pi/2)$	$(-\pi/2,\pi/2)$	12870	90
32	(4,0)	(0,4)	$(\pi/2,0)$	$(0,\pi/2)$	601080390	2970
36	(3,3)	(−3,3)	$(\pi/3,\pi/3)$	$(-\pi/3,\pi/3)$	9075135300	6840
64	(4,4)	(−4,4)	$(\pi/4,\pi/4)$	$(-\pi/4,\pi/4)$	1832624140942590534	2891562
72	(6,0)	(0,6)	$(\pi/3,0)$	$(0,\pi/3)$	442512540276836779204	16448400

where N is the number of lattice sites, $\mathbf{T}_{1,2}$ are the spanning vectors of the cluster, $\mathbf{G}_{1,2}$ are the reciprocal vectors, $\mathcal{D}_{\text{full}}^{S_z=0}$ is the size of the full Hilbert space in the total magnetization $S_z = 0$ sector, and $\mathcal{D}_{\text{spin-ice}}$ is the dimensionality of the spin-ice manifold. Note that, in order to evaluate J_{ij} across the periodic boundaries in a consistent manner [110], we keep the maximum amplitude among the set $\{J_{i,j+\epsilon_1 T_1+\epsilon_2 T_2}, \epsilon_{1,2} = -1,0,1\}$, where $\mathbf{T}_1$ and $\mathbf{T}_2$ are the spanning vectors of the cluster.

APPENDIX F: CLASSICAL MINIMIZATION

Table II summarizes the main results from the classical minimization procedure of Sec. IV C 1 for the finite clusters considered in our ED study but also for the thermodynamic limit (last line). The main findings are as follows: (i) $J_c = 0.3$, *all clusters.*—Here, the minimum sits at $\mathbf{Q} = (\pi,\pi)$, with $\mathbf{v}_1(\mathbf{Q}) = \frac{1}{\sqrt{2}}(1,1)$ and $\lambda_1(\mathbf{Q}) < \lambda_2(\mathbf{Q})$. The minimum energy is achieved by

$$\sigma_{\mathbf{k},\alpha} = \sqrt{2N_{\text{uc}}} v_{1\alpha}(\mathbf{Q})\delta_{\mathbf{k},\mathbf{Q}} \Rightarrow \sigma_{\mathbf{R},\alpha} = \sqrt{2} v_{1\alpha}(\mathbf{Q})e^{i\mathbf{Q}\cdot\mathbf{R}},$$

where $N_{\text{uc}} = N/2$ stands for the number of unit cells, and the constants have been chosen to satisfy the spin-length

constraint. The energy is given by $E'/N_{\text{uc}} = \lambda_1(\mathbf{Q})$. (ii) $J_c = 0.1$, *all clusters except $N = 36$.*—Here, we have two optimal wave vectors, $\mathbf{Q}_1 = (0,\pi)$ and $\mathbf{Q}_2 = (\pi,0)$, with $\lambda_1(\mathbf{Q}_1) = \lambda_1(\mathbf{Q}_2)$ and $v_1(\mathbf{Q}_1) = (1,0)$, $v_1(\mathbf{Q}_2) = (0,1)$, and $\lambda_1(\mathbf{Q}_j) < \lambda_2(\mathbf{Q}_j)$. Then, the solutions that satisfy the spin-length constraint are

$$\sigma_{\mathbf{R},1} = \pm e^{i\mathbf{Q}_1\cdot\mathbf{R}}, \qquad \sigma_{\mathbf{R},2} = \pm e^{i\mathbf{Q}_2\cdot\mathbf{R}};$$

i.e., we have four ground states, with energy $E'/N_{\text{uc}} = \lambda_1(\mathbf{Q}_1)$. (iii) $J_c \leq 0.01$, *all clusters except $N = 36$ and 72.*—Here, the minima sit at $\pm\mathbf{Q} = \pm(-\pi/2,\pi/2)$, with eigenvectors $\mathbf{v}_1(\mathbf{Q}) = (1,\mp i)/\sqrt{2}$, and again $\lambda_1(\mathbf{Q}) < \lambda_2(\mathbf{Q})$. Let us try the ansatz

$$\sigma_{\mathbf{k},\alpha} = \frac{\sqrt{N_{\text{uc}}}}{\sqrt{2}}(v_{1\alpha}(\mathbf{Q})\delta_{\mathbf{k},\mathbf{Q}} + v_{1\alpha}^*(\mathbf{Q})\delta_{\mathbf{k},-\mathbf{Q}})$$

$$\Rightarrow \sigma_{\mathbf{R},\alpha} = \frac{1}{\sqrt{2}}[v_{1\alpha}(\mathbf{Q})e^{i\mathbf{Q}\cdot\mathbf{R}} + v_{1\alpha}(-\mathbf{Q})e^{-i\mathbf{Q}\cdot\mathbf{R}}]$$

$$= \sqrt{2}\,\text{Re}[v_{1\alpha}(\mathbf{Q})e^{i\mathbf{Q}\cdot\mathbf{R}}]$$

$$= \left(\cos(m-n)\frac{\pi}{2}, \sin(m-n)\frac{\pi}{2}\right),$$

where we labeled $\mathbf{R} = n\,\mathbf{e}_x + m\,\mathbf{e}_y$, and n, m are integers. This ansatz does not satisfy the spin-length constraint at all sites. Another ansatz is $\sigma_{\mathbf{R},\alpha} = (-\sin(m-n)\pi/2, \cos(m-n)\pi/2)$, which results from the first ansatz by replacing $\mathbf{v}_1(\mathbf{Q}) \to i\,\mathbf{v}_1(\mathbf{Q})$. To get a solution that satisfies the spin constraint, we combine the two:

$$\sigma_{\mathbf{k},\alpha} = \frac{\sqrt{N_{\mathrm{uc}}}}{\sqrt{2}}\left((\epsilon_1 + i\epsilon_2)v_{1\alpha}(\mathbf{Q})\delta_{\mathbf{k},\mathbf{Q}} + (\epsilon_1 - i\epsilon_2)v_{1\alpha}^*(\mathbf{Q})\delta_{\mathbf{k},-\mathbf{Q}}\right)$$

$$\Rightarrow \sigma_{\mathbf{R},\alpha} = \frac{1}{\sqrt{2}}\left[(\epsilon_1 + i\epsilon_2)v_{1\alpha}(\mathbf{Q})e^{i\mathbf{Q}\cdot\mathbf{R}} + (\epsilon_1 - i\epsilon_2)v_{1\alpha}(-\mathbf{Q})e^{-i\mathbf{Q}\cdot\mathbf{R}}\right] = \sqrt{2}\,\mathrm{Re}[(\epsilon_1 + i\epsilon_2)v_{1\alpha}(\mathbf{Q})e^{i\mathbf{Q}\cdot\mathbf{R}}]$$

$$= \left(\epsilon_1 \cos(m-n)\frac{\pi}{2} - \epsilon_2 \sin(m-n)\frac{\pi}{2}, \epsilon_1 \sin(m-n)\frac{\pi}{2} + \epsilon_2 \cos(m-n)\frac{\pi}{2}\right),$$

where $\epsilon_{1,2} = \pm 1$; i.e., we have four possible solutions, all with energy $E'/N_{\mathrm{uc}} = \lambda_1(\mathbf{Q})$. (iv) *All remaining cases.*— Here, we cannot satisfy the spin-length constraint. This is what happens, e.g., for $N = 36$ and $J_c \leq 0.1$, for $N = 72$ and $J_c \leq 0.01$, and for $N = \infty$ and $J_c \leq 0.01$. In these cases, $\lambda_1(Q)$ serves only as a lower bound of the energy (see comparison with ED data in Table II). From these results, we can infer that the best choice for the cutoff is 0.001, and the best finite-size cluster for the investigation of the $t = 0$ ground states is the $N = 64$ cluster, whose ground-state energy per unit cell, $E'/N_{\mathrm{uc}} = -2.108984$, is very close to the one for $N = \infty$ ($E'/N_{\mathrm{uc}} = -2.11938$). The next good cluster (again in terms of energy) is $N = 32$, which has $E'/N_{\mathrm{uc}} = -2.056628$.

APPENDIX G: TECHNICAL DETAILS ON CLASSICAL MONTE CARLO SIMULATIONS

Low-energy configurations are generated by thermal annealing consisting of a million sweeps per site, using a combination of single-spin flip and long-loop updates. The former can annihilate all types of defects (3 up - 1 down, 3 down - 1 up, 4-up, and 4-down) but suffers from very low acceptance ratios at low temperatures, while the loop updates have much higher acceptance ratios (around 16%) and can annihilate all defects except the 3 up - 1 down (or 3 down - 1 up). So, combining both types of updates gives sufficiently large acceptance ratios and can annihilate all defects.

APPENDIX H: ENERGY SCALES AND POSSIBLE EFFECTS OF DISSIPATION

Here, we briefly comment on other possible imperfections of Rydberg experiments.

Energy scales and state preparation.—The large energy scales provided by dressed Rydberg interactions allow us to engineer RVB plaquette solids with gaps of order of a few hundred Hz. Those are 1 order of magnitude larger than typical exchange energy scales currently employed in bosonic cold-atom experiments, allowing for the investigation of ground-state physics within current temperature regimes.

Beyond a direct cooling within the gauge-invariant manifold protected by such energy scales, the plaquette RVB solid can also be reached via an adiabatic ramp. A first possibility consists of starting directly in the solid phase at $J_\perp = 0$ and switching on the tunneling adiabatically (which corresponds to lowering the optical lattice potential). The ramp has to be performed sufficiently slowly with respect to the energy gap in Fig. 8 in order to limit the number of proliferating defects. Alternatively, adiabatic engineering of small RVB samples has already been experimentally demonstrated in coupled double-well systems [111]: Starting from such a state, one could melt the different RVB cells following a similar procedure as in Ref. [112], that is, merging the different cells by using an additional pair of superlattice potentials in the x-y plane. A possible drawback is represented by spontaneous emission described in Sec. III, which, despite being strongly suppressed by the dressing technique, might still play a detrimental role in establishing the correct ground-state physics. A straightforward way to further minimize the effects of losses would be to address Rydberg p states with higher principal quantum number n, as interactions ($\sim n^{11}$) and decay times ($\sim n^3$) both scale favorably as a function of the principal quantum number. Next, we comment on the expected influence of gauge-variant dissipative dynamics.

For, e.g., $n = 32$, the diagonal interaction between both atoms in the $m_j = 3/2$ state is $V_{\frac{33}{22}}(a) = 2\pi \cdot 150.53$ MHz, while the largest off-diagonal matrix element is $V_{\mathrm{off}}(a) = 2\pi \cdot 65.40$ MHz. Using an AC-Stark laser with $P = 10$ mW, one obtains a Rabi frequency of $\Omega_{AC} = 2\pi \cdot 325$ MHz $\gg V_{\mathrm{off}}(a)$ on the $32P_{3/2} - 7D_{3/2}$ transition. The same laser creates an AC-Stark effect on the ground state 5S of $V_{AC} = 2\pi \cdot 279.5$ kHz, which has to be smaller than the actual lattice trapping the atoms, V_{trap}. The optimal dressed potentials (with respect to NNN imperfections) are obtained with a detuning $\Delta_r = 2\pi \cdot 2475$ kHz (which sets the Condon radius of the steplike interaction) of the Rydberg laser coupling $5S - 32P$. The decay rate of $32P$ is $\Gamma = 2\pi \cdot 2.4$ kHz. With a Rabi frequency of

$\Omega_r = 2\pi \cdot (500, 625, 750)$ kHz, one obtains $\epsilon = \Omega/2\Delta = (0.10, 0.13, 0.15)$. The effective decay rate is $\epsilon^2\Gamma = 2\pi \cdot (24, 38, 55)$ Hz, and the soft-core potential is $\tilde{V}_0 = \epsilon^3\Omega = 2\pi \cdot (515, 1258, 2610)$ Hz. While in this specific case direct tunneling will be suppressed because of the deep lattice potential, one could, nevertheless, demonstrate experimentally the classical order-by-disorder mechanism discussed in Sec. V or exploit internal spin exchange within the Rydberg manifold [77].

Effects of spontaneous emission.—The influence of dissipative dynamics which explicitly violates Gauss constraints has been numerically investigated in Ref. [113] for a series of both Abelian and non-Abelian discrete gauge theories in one dimension. In particular, when the energy scales of dissipative and coherent dynamics are well separate, the influence of dissipative effects is quantitatively negligible as long as low-order observables, such as, e.g., correlation functions, are considered (as is the case here). Because of the stability of the plaquette order (protected by a large energy gap) with respect to Hamiltonian imperfection, we expect a similar stability in the gauge theory studied here. A detailed numerical study on the specific model could shed further light on the effects of spontaneous emission, furthering the understanding on how the low-energy physics affects the open-system dynamics (along the lines discussed in Ref. [114]).

[1] L. Pauling, *The Structure and Entropy of Ice and of Other Crystals with Some Randomness of Atomic Arrangement*, J. Am. Chem. Soc. **57**, 2680 (1935).

[2] W. F. Giauque and M. F. Ashley, *Molecular Rotation in Ice at 10 K. Free Energy of Formation and Entropy of Water*, Phys. Rev. **43**, 81 (1933); W. F. Giauque and J. W. Stout, *The Entropy of Water and the Third Law of Thermodynamics. The Heat Capacity of Ice from 15 to 273 K*, J. Am. Chem. Soc. **58**, 1144 (1936).

[3] E. Lieb, *Exact Solution of the Problem of the Entropy of Two-Dimensional Ice*, Phys. Rev. Lett. **18**, 692 (1967).

[4] M. J. Harris, S. T. Bramwell, D. F. McMorrow, T. Zeiske, and K. W. Godfrey, *Geometrical Frustration in the Ferromagnetic Pyrochlore* $Ho_2Ti_2O_7$, Phys. Rev. Lett. **79**, 2554 (1997).

[5] P. W. Anderson, *Ordering and Antiferromagnetism in Ferrites*, Phys. Rev. **102**, 1008 (1956).

[6] S. T. Bramwell and M. J. P. Gingras, *Spin Ice State in Frustrated Magnetic Pyrochlore Materials*, Science **294**, 1495 (2001).

[7] L. Balents, *Spin Liquids in Frustrated Magnets*, Nature (London) **464**, 199 (2010).

[8] C. Lacroix, P. Mendels, and F. Mila, *Introduction to Frustrated Magnetism: Materials, Experiments, Theory*, Springer Series in Solid-State Sciences (Springer, Berlin, Heidelberg, 2011).

[9] C. Castelnovo, R. Moessner, and S. L. Sondhi, *Magnetic Monopoles in Spin Ice*, Nature (London) **451**, 42 (2008).

[10] R. Moessner and S. L. Sondhi, *Ising Models of Quantum Frustration*, Phys. Rev. B **63**, 224401 (2001).

[11] R. Moessner, O. Tchernyshyov, and S. L. Sondhi, *Planar Pyrochlore, Quantum Ice and Sliding Ice*, J. Stat. Phys. **116**, 755 (2004).

[12] M. Hermele, M. P. A. Fisher, and L. Balents, *Pyrochlore Photons: The $U(1)$ Spin Liquid in a $S = 1/2$ Three-Dimensional Frustrated Magnet*, Phys. Rev. B **69**, 064404 (2004).

[13] A. Banerjee, S. V. Isakov, K. Damle, and Y. Baek Kim, *Unusual Liquid State of Hard-Core Bosons on the Pyrochlore Lattice*, Phys. Rev. Lett. **100**, 047208 (2008).

[14] N. Shannon, O. Sikora, F. Pollmann, K. Penc, and P. Fulde, *Quantum Ice: A Quantum Monte Carlo Study*, Phys. Rev. Lett. **108**, 067204 (2012).

[15] R. Moessner and S. L. Sondhi, *Resonating Valence Bond Phase in the Triangular Lattice Quantum Dimer Model*, Phys. Rev. Lett. **86**, 1881 (2001).

[16] G. Misguich, D. Serban, and V. Pasquier, *Quantum Dimer Model on the Kagome Lattice: Solvable Dimer-Liquid and Ising Gauge Theory*, Phys. Rev. Lett. **89**, 137202 (2002).

[17] R. Moessner and S. L. Sondhi, *Three-Dimensional Resonating-Valence-Bond Liquids and Their Excitations*, Phys. Rev. B **68**, 184512 (2003).

[18] C. L. Henley, *Power-Law Spin Correlations in Pyrochlore Antiferromagnets*, Phys. Rev. B **71**, 014424 (2005).

[19] C. L. Henley, *The "Coulomb Phase" in Frustrated Systems*, Annu. Rev. Condens. Matter Phys. **1**, 179 (2010).

[20] R. Moessner and K. S. Raman, *Quantum Dimer Models*, in *Introduction to Frustrated Magnetism: Materials, Experiments, Theory* (Springer Berlin Heidelberg, Berlin, Heidelberg, 2011), pp. 437–479.

[21] C. Castelnovo, R. Moessner, and S. L. Sondhi, *Spin Ice, Fractionalization, and Topological Order*, Annu. Rev. Condens. Matter Phys. **3**, 35 (2012).

[22] E. Fradkin, *Field Theories of Condensed Matter Systems*, Advanced Books Classics Series (Cambridge University Press, Cambridge, 1997).

[23] R. Heidemann, U. Raitzsch, V. Bendkowsky, B. Butscher, R. Löw, and T. Pfau, *Rydberg Excitation of Bose-Einstein Condensates*, Phys. Rev. Lett. **100**, 033601 (2008).

[24] W. Anderson, J. Veale, and T. Gallagher, *Resonant Dipole-Dipole Energy Transfer in a Nearly Frozen Rydberg Gas*, Phys. Rev. Lett. **80**, 249 (1998).

[25] C. S. Hofmann, G. Günter, H. Schempp, N. L. M. Müller, A. Faber, H. Busche, M. Robert-de Saint-Vincent, S. Whitlock, and M. Weidemüller, *An Experimental Approach for Investigating Many-Body Phenomena in Rydberg-Interacting Quantum Systems*, Front. Phys. **9**, 571 (2014).

[26] D. Maxwell, D. J. Szwer, D. Paredes-Barato, H. Busche, J. D. Pritchard, A. Gauguet, K. J. Weatherill, M. P. A. Jones, and C. S. Adams, *Storage and Control of Optical Photons Using Rydberg Polaritons*, Phys. Rev. Lett. **110**, 103001 (2013).

[27] A. Schwarzkopf, D. A. Anderson, N. Thaicharoen, and G. Raithel, *Spatial Correlations between Rydberg Atoms in an Optical Dipole Trap*, Phys. Rev. A **88**, 061406 (2013).

[28] H. Schempp, G. Günter, M. Robert-de Saint-Vincent, C. S. Hofmann, D. Breyel, A. Komnik, D. W. Schönleber, M. Gärttner, J. Evers, and S. Whitlock, *Full Counting Statistics of Laser Excited Rydberg Aggregates in a One-Dimensional Geometry*, Phys. Rev. Lett. **112**, 013002 (2014).

[29] A. Tauschinsky, R. M. T. Thijssen, S. Whitlock, H. B. van Linden van den Heuvell, and R. J. C. Spreeuw, *Spatially Resolved Excitation of Rydberg Atoms and Surface Effects on an Atom Chip*, Phys. Rev. A **81**, 063411 (2010).

[30] J. D. Carter and J. D. D. Martin, *Coherent Manipulation of Cold Rydberg Atoms Near the Surface of an Atom Chip*, Phys. Rev. A **88**, 043429 (2013).

[31] H. Kübler, J. P. Shaffer, T. Baluktsian, R. Löw, and T. Pfau, *Coherent Excitation of Rydberg Atoms in Micrometre-Sized Atomic Vapour Cells*, Nat. Photonics **4**, 112 (2010).

[32] Y. O. Dudin and A. Kuzmich, *Strongly Interacting Rydberg Excitations of a Cold Atomic Gas*, Science **336**, 887 (2012).

[33] P. Schauß, M. Cheneau, M. Endres, T. Fukuhara, S. Hild, A. Omran, T. Pohl, C. Gross, S. Kuhr, and I. Bloch, *Observation of Spatially Ordered Structures in a Two-Dimensional Rydberg Gas*, Nature (London) **491**, 87 (2012).

[34] L. Li, Y. O. Dudin, and A. Kuzmich, *Entanglement between Light and an Optical Atomic Excitation*, Nature (London) **498**, 466 (2013).

[35] M. Ebert, A. Gill, M. Gibbons, X. Zhang, M. Saffman, and T. G. Walker, *Atomic Fock State Preparation Using Rydberg Blockade*, Phys. Rev. Lett. **112**, 043602 (2014).

[36] M. M. Valado, N. Malossi, S. Scotto, D. Ciampini, E. Arimondo, and O. Morsch, *Rydberg Tomography of an Ultracold Atomic Cloud*, Phys. Rev. A **88**, 045401 (2013).

[37] D. Barredo, S. Ravets, H. Labuhn, L. Béguin, A. Vernier, F. Nogrette, T. Lahaye, and A. Browaeys, *Demonstration of Strong Rydberg Blockade in Three-Atom Systems with Anisotropic Interactions*, Phys. Rev. Lett. **112**, 183002 (2014).

[38] J. Dalibard, F. Gerbier, G. Juzeliūnas, and P. Öhberg, *Colloquium: Artificial Gauge Potentials for Neutral Atoms*, Rev. Mod. Phys. **83**, 1523 (2011).

[39] S. Tewari, V. W. Scarola, T. Senthil, and S. Das Sarma, *Emergence of Artificial Photons in an Optical Lattice*, Phys. Rev. Lett. **97**, 200401 (2006).

[40] D. Banerjee, M. Bögli, M. Dalmonte, E. Rico, P. Stebler, U. J. Wiese, and P. Zoller, *Atomic Quantum Simulation of $U(N)$ and $SU(N)$ Non-Abelian Lattice Gauge Theories*, Phys. Rev. Lett. **110**, 125303 (2013).

[41] L. Tagliacozzo, A. Celi, A. Zamora, and M. Lewenstein, *Optical Abelian Lattice Gauge Theories*, Ann. Phys. (Amsterdam) **330**, 160 (2013).

[42] E. Zohar, J. Ignacio Cirac, and B. Reznik, *Cold-Atom Quantum Simulator for $SU(2)$ Yang-Mills Lattice Gauge Theory*, Phys. Rev. Lett. **110**, 125304 (2013).

[43] C. Nisoli, R. Moessner, and P. Schiffer, *Colloquium: Artificial Spin Ice: Designing and Imaging Magnetic Frustration*, Rev. Mod. Phys. **85**, 1473 (2013).

[44] A. Libál, C. Reichhardt, and C. Reichhardt, *Realizing Colloidal Artificial Ice on Arrays of Optical Traps*, Phys. Rev. Lett. **97**, 228302 (2006).

[45] G. Möller and R. Moessner, *Artificial Square Ice and Related Dipolar Nanoarrays*, Phys. Rev. Lett. **96**, 237202 (2006).

[46] T. F. Gallagher, *Rydberg Atoms*, Cambridge Monographs on Atomic, Molecular and Chemical Physics (Cambridge University Press, Cambridge, England, 2005).

[47] M. Saffman, T. G. Walker, and K. Mølmer, *Quantum Information with Rydberg Atoms*, Rev. Mod. Phys. **82**, 2313 (2010).

[48] D. Comparat and P. Pillet, *Dipole Blockade in a Cold Rydberg Atomic Sample*, J. Opt. Soc. Am. B **27**, A208 (2010).

[49] R. Löw, H. Weimer, J. Nipper, J. B. Balewski, B. Butscher, H. Peter Büchler, and T. Pfau, *An Experimental and Theoretical Guide to Strongly Interacting Rydberg Gases*, J. Phys. B **45**, 113001 (2012).

[50] D. Jaksch, J. I. Cirac, P. Zoller, R. Côté, and M. D. Lukin, *Fast Quantum Gates for Neutral Atoms*, Phys. Rev. Lett. **85**, 2208 (2000).

[51] M. D. Lukin, M. Fleischhauer, R. Côté, L. M. Duan, D. Jaksch, J. I. Cirac, and P. Zoller, *Dipole Blockade and Quantum Information Processing in Mesoscopic Atomic Ensembles*, Phys. Rev. Lett. **87**, 037901 (2001).

[52] T. G. Walker and M. Saffman, *Consequences of Zeeman Degeneracy for the van der Waals Blockade between Rydberg Atoms*, Phys. Rev. A **77**, 032723 (2008).

[53] T. G. Walker and M. Saffman, *Zeros of Rydberg–Rydberg Föster Interactions*, J. Phys. B **38**, S309 (2005).

[54] A. Reinhard, T. Liebisch, B. Knuffman, and G. Raithel, *Level Shifts of Rubidium Rydberg States Due to Binary Interactions*, Phys. Rev. A **75**, 032712 (2007).

[55] K. Singer, J. Stanojevic, M. Weidemüller, and R. Côté, *Long-Range Interactions between Alkali Rydberg Atom Pairs Correlated to the ns–ns, np–np and nd–nd Asymptotes*, J. Phys. B **38**, S295 (2005).

[56] L. Santos, G. V. Shlyapnikov, P. Zoller, and M. Lewenstein, *Bose-Einstein Condensation in Trapped Dipolar Gases*, Phys. Rev. Lett. **85**, 1791 (2000).

[57] J. Honer, H. Weimer, T. Pfau, and H. Peter Büchler, *Collective Many-Body Interaction in Rydberg Dressed Atoms*, Phys. Rev. Lett. **105**, 160404 (2010).

[58] G. Pupillo, A. Micheli, M. Boninsegni, I. Lesanovsky, and P. Zoller, *Strongly Correlated Gases of Rydberg-Dressed Atoms: Quantum and Classical Dynamics*, Phys. Rev. Lett. **104**, 223002 (2010).

[59] N. Henkel, R. Nath, and T. Pohl, *Three-Dimensional Roton Excitations and Supersolid Formation in Rydberg-Excited Bose-Einstein Condensates*, Phys. Rev. Lett. **104**, 195302 (2010).

[60] T. Macrì and T. Pohl, *Rydberg Dressing of Atoms in Optical Lattices*, Phys. Rev. A **89**, 011402 (2014).

[61] J. Villain, R. Bidaux, J.-P. Carton, and R. Conte, *Order as an Effect of Disorder*, J. Phys. **41**, 1263 (1980).

[62] E. F. Shender, *Antiferromagnetic Garnets with Fluctuationally Interacting Sublattices*, JETP **56**, 178 (1982).

[63] T. Yildirim, A. B. Harris, and E. F. Shender, *Frustration and Quantum Fluctuations in Heisenberg FCC Antiferromagnets*, Phys. Rev. B **58**, 3144 (1998).

[64] M. Endres, M. Cheneau, T. Fukuhara, C. Weitenberg, P. Schauß, C. Gross, L. Mazza, M. C. Banuls, L. Pollet,

I. Bloch, and S. Kuhr, *Observation of Correlated Particle-Hole Pairs and String Order in Low-Dimensional Mott Insulators*, Science **334**, 200 (2011).

[65] B. Nienhuis, *Two-Dimensional Critical Phenomena and the Coulomb Gas*, in *Phase Transitions and Critical Phenomena*, Vol. 11, edited by C. Domb, M. Green, and J. L. Lebowitz (Academic Press, London, 1987).

[66] C. Zeng and C. L. Henley, *Zero-Temperature Phase Transitions of an Antiferromagnetic Ising Model of General Spin on a Triangular Lattice*, Phys. Rev. B **55**, 14935 (1997).

[67] T. Fukuhara, A. Kantian, M. Endres, M. Cheneau, P. Schauß, S. Hild, D. Bellem, U. Schollwöck, T. Giamarchi, C. Gross, I. Bloch, and S. Kuhr, *Quantum Dynamics of a Mobile Spin Impurity*, Nat. Phys. **9**, 235 (2013).

[68] D. Banerjee, F.-J. Jiang, P. Widmer, and U.-J. Wiese, *The $(2+1)$-d $U(1)$ Quantum Link Model Masquerading as Deconfined Criticality*, J. Stat. Mech. (2013) P12010.

[69] U. J. Wiese, *Ultracold Quantum Gases and Lattice Systems: Quantum Simulation of Lattice Gauge Theories*, Ann. Phys. (Amsterdam) **525**, 777 (2013).

[70] R. Moessner and J. T. Chalker, *Low-Temperature Properties of Classical Geometrically Frustrated Antiferromagnets*, Phys. Rev. B **58**, 12049 (1998).

[71] N. Shannon, G. Misguich, and K. Penc, *Cyclic Exchange, Isolated States, and Spinon Deconfinement in an XXZ Heisenberg Model on the Checkerboard Lattice*, Phys. Rev. B **69**, 220403 (2004).

[72] S. Sachdev, *Quantum Phase Transitions* (Cambridge University Press, Cambridge, England, 2001).

[73] M. Viteau, M. G. Bason, J. Radogostowicz, N. Malossi, D. Ciampini, O. Morsch, and E. Arimondo, *Rydberg Excitations in Bose-Einstein Condensates in Quasi-One-Dimensional Potentials and Optical Lattices*, Phys. Rev. Lett. **107**, 060402 (2011).

[74] P. W. Milonni, *The Quantum Vacuum: An Introduction to Quantum Electrodynamics* (Academic Press, New York, 1994).

[75] J. Schwinger, L. L. J. Deraad, K. A. Milton, and W. Tsai, *Classical Electrodynamics*, Advanced Book Program (Westview Press, Seiten, 1998).

[76] A. Dauphin, M. Müller, and M. A. Martin-Delgado, *Rydberg-Atom Quantum Simulation and Chern-Number Characterization of a Topological Mott Insulator*, Phys. Rev. A **86**, 053618 (2012).

[77] A. W. Glaetzle, M. Dalmonte, R. Nath, C. Gross, I. Bloch, and P. Zoller, *Frustrated Quantum Magnetism with Laser-Dressed Rydberg Atoms*, arXiv:1410.3388.

[78] W. S. Bakr, J. I. Gillen, A. Peng, S. Fölling, and M. Greiner, *A Quantum Gas Microscope for Detecting Single Atoms in a Hubbard-Regime Optical Lattice*, Nature (London) **462**, 74 (2009).

[79] J. F. Sherson, C. Weitenberg, M. Endres, M. Cheneau, I. Bloch, and S. Kuhr, *Single-Atom-Resolved Fluorescence Imaging of an Atomic Mott Insulator*, Nature (London) **467**, 68 (2010).

[80] P. W. Anderson, *Basic Notions of Condensed Matter Physics, Frontiers in Physics*, Vol. 55 (Benjamin Cummings, London, 1984).

[81] B. Bernu, C. Lhuillier, and L. Pierre, *Signature of Néel Order in Exact Spectra of Quantum Antiferromagnets on Finite Lattices*, Phys. Rev. Lett. **69**, 2590 (1992); B. Bernu, P. Lecheminant, C. Lhuillier, and L. Pierre, *Exact Spectra, Spin Susceptibilities, and Order Parameter of the Quantum Heisenberg Antiferromagnet on the Triangular Lattice*, Phys. Rev. B **50**, 10048 (1994).

[82] C. Lhuillier, *Frustrated Quantum Magnets*, arXiv:cond-mat/0502464.

[83] G. Misguich and P. Sindzingre, *Detecting Spontaneous Symmetry Breaking in Finite-Size Spectra of Frustrated Quantum Antiferromagnets*, J. Phys. Condens. Matter **19**, 145202 (2007).

[84] I. Rousochatzakis, A. M. Läuchli, and R. Moessner, *Quantum Magnetism on the Cairo Pentagonal Lattice*, Phys. Rev. B **85**, 104415 (2012).

[85] J. B. Fouet, M. Mambrini, P. Sindzingre, and C. Lhuillier, *Planar Pyrochlore: A Valence-Bond Crystal*, Phys. Rev. B **67**, 054411 (2003).

[86] Such "extra" low-lying states are also present in the pure Heisenberg model and are related to extra symmetries of the 32-site cluster [85].

[87] J. M. Luttinger and L. Tisza, *Theory of Dipole Interaction in Crystals*, Phys. Rev. **70**, 954 (1946).

[88] E. F. Bertaut, *Configurations Magnétiques. Méthode de Fourier*, J. Phys. Chem. Solids **21**, 256 (1961).

[89] D. B. Litvin, *The Luttinger-Tisza Method*, Physica (Amsterdam) **77**, 205 (1974).

[90] T. A. Kaplan and N. Menyuk, *Spin Ordering in Three-Dimensional Crystals with Strong Competing Exchange Interactions*, Philos. Mag. **87**, 3711 (2007).

[91] R. J. Elliott, *Phenomenological Discussion of Magnetic Ordering in the Heavy Rare-Earth Metals*, Phys. Rev. **124**, 346 (1961).

[92] M. Fisher and W. Selke, *Infinitely Many Commensurate Phases in a Simple Ising Model*, Phys. Rev. Lett. **44**, 1502 (1980).

[93] P. Bak, *Commensurate Phases, Incommensurate Phases and the Devil's Staircase*, Rep. Prog. Phys. **45**, 587 (1982).

[94] W. Selke, *The ANNNI Model-Theoretical Analysis and Experimental Application*, Phys. Rep. **170**, 213 (1988).

[95] W. Krauth and R Moessner, *Pocket Monte Carlo Algorithm for Classical Doped Dimer Models*, Phys. Rev. B **67**, 064503 (2003).

[96] C. Carr, R. Ritter, C. G. Wade, C. S. Adams, and K. J. Weatherill, *Nonequilibrium Phase Transition in a Dilute Rydberg Ensemble*, Phys. Rev. Lett. **111**, 113901 (2013).

[97] Sergei V. Isakov, R. Moessner, and S. L. Sondhi, *Why Spin Ice Obeys the Ice Rules*, Phys. Rev. Lett. **95**, 217201 (2005).

[98] This is the case, e.g., of the Kagome Bose-Hubbard model with the hexagonal cell as a gauge cell, where the proper low-energy theory is a $\mathbb{Z}_2$ gauge theory that can undergo deconfinement and thus stabilize a spin-liquid phase.

[99] J. Richter, J. Schulenburg, and A. Honecker, *Quantum Magnetism in Two Dimensions: From Semi-classical Néel Order to Magnetic Disorder*, in *Quantum Magnetism*, edited by U. Schollwöck, J. Richter, D. J. J. Farnell, and R. F. Bishop (Springer, Berlin, Heidelberg, 2004), pp. 85–153.

[100] R. Siddharthan and A. Georges, *Square Kagome Quantum Antiferromagnet and the Eight-Vertex Model*, Phys. Rev. B

65, 014417 (2001); P. Tomczak and J. Richter, *Thermo-dynamical Properties of the Heisenberg Antiferromagnet on the Kagomé Lattice*, Phys. Rev. B **54,** 9004 (1996).

[101] I. Rousochatzakis, R. Moessner, and J. van den Brink, *Frustrated Magnetism and Resonating Valence Bond Physics in Two-Dimensional Kagome-like Magnets*, Phys. Rev. B **88,** 195109 (2013).

[102] D. C. Cabra, M. D. Grynberg, P. C. W. Holdsworth, A. Honecker, P. Pujol, J. Richter, D. Schmalfuß, and J. Schulenburg, *Quantum Kagomé Antiferromagnet in a Magnetic Field: Low-Lying Nonmagnetic Excitations Versus Valence-Bond Crystal Order*, Phys. Rev. B **71,** 144420 (2005).

[103] D. L. Bergman, R. Shindou, G. A. Fiete, and L. Balents, *Degenerate Perturbation Theory of Quantum Fluctuations in a Pyrochlore Antiferromagnet*, Phys. Rev. B **75,** 094403 (2007).

[104] I. Rousochatzakis, A. M Läuchli, and F. Mila, *Highly Frustrated Magnetic Clusters: The Kagomé on a Sphere*, Phys. Rev. B **77,** 094420 (2008).

[105] D. Banerjee, M. Dalmonte, M. Müller, E. Rico, P. Stebler, U. J. Wiese, and P. Zoller, *Atomic Quantum Simulation of Dynamical Gauge Fields Coupled to Fermionic Matter: From String Breaking to Evolution after a Quench*, Phys. Rev. Lett. **109,** 175302 (2012).

[106] P. A. Lee, N. Nagaosa, and X.-G. Wen, *Doping a Mott Insulator: Physics of High-Temperature Superconductivity*, Rev. Mod. Phys. **78,** 17 (2006).

[107] E. Fradkin and S. Shenker, *Phase Diagrams of Lattice Gauge Theories with Higgs Fields*, Phys. Rev. D **19,** 3682 (1979).

[108] Y. Wan and O. Tchernyshyov, *Quantum Strings in Quantum Spin Ice*, Phys. Rev. Lett. **108,** 247210 (2012).

[109] M. Marinescu, H. Sadeghpour, and A. Dalgarno, *Dispersion Coefficients for Alkali-Metal Dimers*, Phys. Rev. A **49,** 982 (1994).

[110] It is not enough to choose the minimum distance as a criterion since it may happen that the distance between i and j and, e.g., that between i and $j + \mathbf{T}_1$ is the same, but the corresponding amplitudes are not the same.

[111] S. Nascimbène, Y.-A. Chen, M. Atala, M. Aidelsburger, S. Trotzky, B. Paredes, and I. Bloch, *Experimental Realization of Plaquette Resonating Valence Bond States with Ultracold Atoms in Optical Superlattices*, Phys. Rev. Lett. **108,** 205301 (2012).

[112] S. Trebst, U. Schollwoeck, M. Troyer, and P. Zoller, *d-wave Resonating Valence Bond States of Fermionic Atoms in Optical Lattices*, Phys. Rev. Lett. **96,** 250402 (2006).

[113] K. Stannigel, P. Hauke, D. Marcos, M. Hafezi, S. Diehl, M. Dalmonte, and P. Zoller, *Constrained Dynamics via the Zeno Effect in Quantum Simulation: Implementing Non-Abelian Lattice Gauge Theories with Cold Atoms*, Phys. Rev. Lett. **112,** 120406 (2014).

[114] J. Schachenmayer, L. Pollet, M. Troyer, and A. John Daley, *Spontaneous Emissions and Thermalization of Cold Bosons in Optical Lattices*, Phys. Rev. A **89,** 011601 (2014).